

1 **Targeting DHX9 triggers tumor-intrinsic interferon response and replication stress in**  
2 **Small Cell Lung Cancer**

3  
4 **Authors:** Takahiko Murayama<sup>1,2,3</sup>, Jun Nakayama<sup>4,5</sup>, Xinpei Jiang<sup>1,2,3,6</sup>, Kenichi Miyata<sup>7,8</sup>,  
5 Alexander D. Morris<sup>1,2</sup>, Kathy Q. Cai<sup>9</sup>, Rahul M. Prasad<sup>1</sup>, Xueying Ma<sup>1,2,3</sup>, Andrey Efimov<sup>10</sup>,  
6 Neel Belani<sup>11</sup>, Emily R. Gerstein<sup>1,2</sup>, Yinfei Tan<sup>12</sup>, Yan Zhou<sup>13</sup>, William Kim<sup>14,15,16</sup>, Reo  
7 Maruyama<sup>7,17</sup>, Kerry S. Campbell<sup>1,2,3</sup>, Lu Chen<sup>1,2</sup>, Yibin Yang<sup>1,2,3</sup>, Siddharth Balachandran<sup>3,18</sup>,  
8 Israel Cañadas<sup>1,2,3\*</sup>

9  
10 <sup>1</sup>Nuclear Dynamics and Cancer Program, Fox Chase Cancer Center, Philadelphia, PA, USA

11 <sup>2</sup>Cancer Epigenetics Institute, Fox Chase Cancer Center, Philadelphia, PA, USA

12 <sup>3</sup>Center for Immunology, Fox Chase Cancer Center, Philadelphia, PA, USA

13 <sup>4</sup>Laboratory of Integrative Oncology, National Cancer Center Research Institute, Tokyo, Japan

14 <sup>5</sup>Department of Oncogenesis and Growth Regulation, Research Institute, Osaka International  
15 Cancer Institute, Osaka, Japan

16 <sup>6</sup>Biomedical Science Graduate Program, Lewis Katz School of Medicine at Temple University,  
17 Philadelphia, PA, USA

18 <sup>7</sup>Project for Cancer Epigenomics, Cancer Institute, Japanese Foundation for Cancer Research,  
19 Tokyo, Japan

20 <sup>8</sup>Cancer Cell Communication Project, NEXT-Ganken Program, Japanese Foundation for Cancer  
21 Research, Tokyo, Japan

22 <sup>9</sup>Histopathology Facility, Fox Chase Cancer Center, Philadelphia, PA, USA

23 <sup>10</sup>Bio Imaging Facility, Fox Chase Cancer Center, Philadelphia, PA, USA

24 <sup>11</sup>Department of Medical Oncology, Fox Chase Cancer Center, Philadelphia, PA, USA

25 <sup>12</sup>Genomics Facility, Fox Chase Cancer Center, Philadelphia, PA, USA

26 <sup>13</sup>Biostatistics and Bioinformatics Facility, Fox Chase Cancer Center, Philadelphia, PA, USA

27 <sup>14</sup>Moore's Cancer Center, UC San Diego, La Jolla, CA, USA

28 <sup>15</sup>Center for Novel Therapeutics, UC San Diego, La Jolla, CA, USA

29 <sup>16</sup>Department of Medicine, UC San Diego, La Jolla, CA, USA

30 <sup>17</sup>Cancer Cell Diversity Project, NEXT-Ganken Program, Japanese Foundation for Cancer  
31 Research, Tokyo, Japan

32 <sup>18</sup>Cancer Signaling and Microenvironment Program, Fox Chase Cancer Center, Philadelphia, PA,  
33 USA

34  
35 **Corresponding Author**

36 Israel Cañadas, Ph.D.

37 333 Cottman Avenue, Philadelphia, PA 19111

38 Email; [israel.canadas@fccc.edu](mailto:israel.canadas@fccc.edu)

39 Phone; +1 215-214-1572

40

41 **Running Title**

42 Targeting DHX9 induces IFN response and replication stress

43

44 **Disclosure of Potential Conflicts of Interest**

45 The authors declare no Conflicts of Interest.

46

47 **Key words**

48 Small cell lung cancer, tumor-intrinsic innate immunity, DHX9

49

50 **Financial support**

51 This research was supported, in part, by grants (to I.C.) from the Lung Cancer Research

52 Foundation, the G. Harold and Leila Y. Mathers Foundation, the W. W. Smith Charitable Trust

53 and the Bucks County Chapter of the Board of Associates of Fox Chase Cancer Center.

54 Additional funding was provided by a Grant-in-Aid for a Japan Society for Promotion of Science

55 (JSPS) fellowship to T.M. (202160224; <http://www.jsps.go.jp/english/e-pd/index.html>). This

56 research was also supported by NIH grants R35GM150538 (to L.C.) and T32GM142606 training

57 fellowship to (X.J.)

58

59

60

61 **Abstract**

62 Activating innate immunity in cancer cells through cytoplasmic nucleic acid sensing pathways,  
63 a phenomenon known as “viral mimicry”, has emerged as an effective strategy to convert  
64 immunologically “cold” tumors into “hot”. Through a curated CRISPR-based screen of RNA  
65 Helicases, we identified DExD/H-box helicase 9 (DHX9) as a potent repressor of double-stranded  
66 RNA (dsRNA) in small cell lung cancers (SCLCs). Depletion of DHX9 induced accumulation of  
67 cytoplasmic dsRNA and triggered tumor-intrinsic innate immunity. Intriguingly, ablating DHX9  
68 also induced aberrant accumulation of R-loops, which resulted in an increase of DNA  
69 damage-derived cytoplasmic DNA and replication stress in SCLCs. *In vivo*, DHX9 deletion  
70 promoted decrease in tumor growth while inducing a more immunogenic tumor  
71 microenvironment, invigorating responsiveness to immune checkpoint blockade. These findings  
72 suggest that DHX9 is a crucial repressor of tumor-intrinsic innate immunity and replication stress,  
73 representing a promising target for SCLC and other “cold” tumors where genomic instability  
74 contribute to pathology.

75

76

77

78 **Significance**

79 One promising strategy to trigger an immune response within tumors and enhance  
80 immunotherapy efficacy is by inducing endogenous “virus-mimetic” nucleic acids accumulation.  
81 Here, we identify DHX9 as a viral-mimicry-inducing factor involved in the suppression of  
82 double-stranded RNAs and R-loops, and propose DHX9 as a novel target to enhance antitumor  
83 immunity.

84

85

## 86 **Introduction**

87 Activating innate immunity in cancer cells is a potent means by which cold (“immune-desert”  
88 or “immune-excluded”) tumors can be turned hot (“immune-inflamed”, where T cells and other  
89 immune cells are positioned near the tumor cells), enhancing responsiveness to immune  
90 checkpoint blockade (ICB) therapies (1-5). One promising strategy to trigger an innate immune  
91 response within tumors and boost cancer immunotherapy is by inducing the intracellular  
92 accumulation of endogenous “virus-mimetic” nucleic acids, including double-stranded RNAs  
93 (dsRNA) and double-stranded DNAs (dsDNA) (6-9). These nucleic acids are sensed by the host  
94 innate immune system as evidence of viral replication, and provoke an immediate and robust  
95 IFN-driven antiviral response (10,11). Such an antiviral response is potently immunogenic, and  
96 viral mimicry inducing therapies have shown very promising results in pre-clinical models  
97 (6,9-13) and in clinical trials (14,15).

98 Small cell lung cancer (SCLC), the most lethal type of lung cancer, is a classic example of a  
99 cold tumor. While having one of the highest mutational burdens because of its strong association  
100 with tobacco smoking, SCLC is characterized by a reduced antigen presentation and an  
101 immunologically desert tumor microenvironment (TME) (16-18). Despite the addition of ICB  
102 therapy to standard platinum-based chemotherapy in first-line treatment, SCLC remains a  
103 devastating disease and only a minority of SCLC patients derive lasting benefit from these  
104 treatments (19-22). Recent studies analyzing murine and human SCLC tumors suggest the  
105 existence of an “inflamed” SCLC subtype characterized by high expression of immune-related  
106 genes and human leukocyte antigens (HLAs) and exhibits the greatest benefit from ICB therapy  
107 among all the SCLC subtypes (9,23,24). This emphasizes the urgent need to identify novel  
108 therapeutic targets able to enhance antitumor immunity and ultimately sensitize these cold tumors  
109 to immunotherapies.

110 Although SCLCs have been uniformly treated with DNA damaging platinum-based  
111 chemotherapy, recent studies have demonstrated the potential of replication stress inducers as a  
112 therapeutic strategy for SCLC tumors (12,13,25), including inhibitors of poly (ADP-ribose)  
113 polymerase (PARP) and checkpoint kinase 1 (CHK1). These inhibitors block the DNA damage  
114 response (DDR) pathway to induce replication stress and cell death in cancer cells whose genome  
115 is instable because of mutations in DDR pathway genes and/or dysregulated cell cycle  
116 progression. Recently, PARP, CHK1 and WEE1 inhibitors have been reported to work in synergy  
117 with PD-1/PD-L1 blockade in SCLC (26,27), as well as triple negative breast cancer (28) and  
118 ovarian cancer (29). PARP or CHK1 inhibition induces cyclic GMP-AMP synthase  
119 (cGAS)-stimulator of interferon genes (STING) pathway activation, which senses cytoplasmic  
120 DNA generated by DNA damage, activating tumor-intrinsic innate immunity (26).

121 In the current study, we undertook a discovery effort to identify critical regulators of dsRNA in  
122 SCLC cells through a curated CRISPR-based screen of RNA helicases, and identified the  
123 DExD/H-box helicase 9 (DHX9) as a promising strategy by which viral mimicry can be triggered  
124 in immunologically cold tumors. DHX9 is an abundant RNA/DNA helicase capable of unwinding  
125 both RNA and DNA duplexes, as well as more complex nucleic acid structures (30,31). Its  
126 functions include regulation of transcription, RNA processing and transport, and maintenance of  
127 genomic stability (32). We demonstrate that DHX9 suppresses the accumulation of dsRNAs as  
128 well as R-loops (DNA/RNA hybrids), and its depletion leads not only to an antiviral immune  
129 response, but also to DNA replication stress and DNA damage in SCLC cells. DHX9 deletion  
130 causes a dramatic decrease in cancer cell viability *in vitro* and promotes increased  
131 immunogenicity in mouse models of SCLC, significantly enhancing ICB responsiveness. These  
132 findings provide the first description of the role of DHX9 on tumor immunity and genomic  
133 instability, and the identification of a novel viral mimicry-inducing strategy to enhance antitumor  
134 immunity and boost cancer immunotherapy in immunologically cold tumors, such as SCLC.  
135  
136

## 137 **Results**

### 138 **DHX9 suppresses double-stranded RNA (dsRNA) accumulation in SCLCs**

139 Previous studies have revealed that some RNA helicases have the ability of unwinding dsRNA  
140 structures (31,33,34). Thus, we hypothesized that targeting RNA helicases would be a novel and  
141 efficient strategy to induce innate immune response through dsRNA accumulation in cold tumors.  
142 To identify RNA helicases whose function are critical for dsRNA unwinding in SCLC cells, we  
143 performed a curated flow cytometry-based CRISPR screen that detected levels of intracellular  
144 dsRNA in SCLC cells (Fig. 1A and B). We included sgRNAs targeting 32 different genes  
145 (Supplementary Table S1) which have been reported to work as RNA helicases and to contribute  
146 to RNA-related functions including splicing, nuclear export, cytoplasmic transport, translation  
147 regulation and mRNA degradation (35). We used H446 SCLC cell line because it showed the  
148 potential to strongly increase endogenous dsRNA after treatment with Decitabine, a  
149 DNA-methyltransferase inhibitor reported to induce dsRNA accumulation in cancer cells (10)  
150 (Supplementary Fig. S1A). Among the top hit candidates of the screen (Fig. 1B),  
151 sgRNA-mediated depletion of the DExD/H-box helicase 9 (DHX9) significantly increased  
152 dsRNA. Intriguingly, the tumor type with the highest expression of DHX9 levels among all the  
153 tumor types registered in Cancer Cell Line Encyclopedia (CCLE) database was SCLC (Fig. 1C).  
154 Indeed, most SCLC cell lines exhibited high expression of DHX9 at protein level (Supplementary  
155 Fig. S1B). To investigate the relevance of DHX9 in human SCLC and other tumor types, we  
156 interrogated transcriptomic data from public cancer datasets, including The Cancer Genome Atlas  
157 (TCGA). Importantly, DHX9 overexpression was observed in many human lung cancer types  
158 compared to normal lung, and SCLC showed the strongest DHX9 expression among all the lung  
159 cancer subtypes (Fig. 1D), consistent with the CCLE analysis (Fig. 1C). Together, these results  
160 suggest that DHX9 would be a promising target of SCLC. Next, we sought to investigate the  
161 relevance of DHX9 expression on patient survival. Kaplan-Meier analysis of lung tumor patients,  
162 as well as other tumor types including ovarian and breast cancers, revealed that high DHX9  
163 expression was associated with poor patient prognosis (Fig. 1E; Supplementary Fig. S1C), which  
164 is consistent with previous reports on prostate cancer and hepatocellular carcinoma patients  
165 (36,37).

166 Recently, DHX9 has been demonstrated to bind directly to short interspersed nuclear element  
167 (SINE) Alu elements, which could be a source of dsRNA and circular RNA (circRNA) (38). This  
168 finding may implicate DHX9 as an important mediator of cellular dsRNA. To validate the finding  
169 of the screen, we depleted DHX9 by two different sgRNA sequences (sgDHX9 and sgDHX9 #2)  
170 in H446 cells (Fig. 1F) and tested dsRNA accumulation by immunofluorescence (IF) staining  
171 using a dsRNA-specific antibody (J2 antibody). Cells lacking DHX9 showed an accumulation of  
172 cytoplasmic dsRNA when stained with J2 antibody. Furthermore, the J2 signal was efficiently

173 diminished by dsRNA-specific RNase III treatment, suggesting that the J2 antibody is specifically  
174 recognizing dsRNAs (Fig. 1G). We depleted DHX9 in additional SCLC cell lines (H196, H82  
175 and DMS-114) and confirmed accumulation of dsRNA by intracellular flow cytometry in all the  
176 SCLC cell lines tested (Supplementary Fig. S1D and S1E).

177 Previous studies reported that the source of immunogenic dsRNAs generated in cancer cells  
178 treated with certain epigenetic inhibitors were various endogenous retroviral elements (EREs)  
179 subtypes, including SINEs, long interspersed nuclear elements (LINEs) and long terminal repeats  
180 (LTRs) (10,39,40). To identify the genomic sources of dsRNA accumulated in DHX9 depleted  
181 cells, we used J2 antibody to immunoprecipitate dsRNAs in DHX9 depleted SCLC cells and  
182 performed RNA Immunoprecipitation Sequencing (RIP-seq). Sequencing J2-enriched RNAs  
183 showed that the dsRNAs derived from LINE and SINE families were strongly increased in  
184 sgDHX9 cells (Fig. 1H), indicating that DHX9 plays an important role in unwinding LINE and  
185 SINE-derived dsRNA structures in SCLC cells. Also, dsRNAs from LTR families were  
186 significantly increased in sgDHX9 cells (Fig. 1H; Supplementary Fig. S1F). In addition, J2-RIP  
187 experiments followed by quantitative RT-PCR (qRT-PCR) analysis confirmed that DHX9  
188 depletion increased the dsRNAs derived from various ERE subfamilies, including SINEs (Alu),  
189 LTR-ERVs (HERV-K) and satellite repeats (SAT III), as well as LINEs (L1 ORFs) (Fig. 1I).

190 We next wanted to understand which nucleic acid sensors were involved in the recognition of  
191 the dsRNAs accumulated in DHX9 depleted cells, as well as the specific genomic sources of  
192 dsRNAs recognized by these sensors. Since both MDA5 and RIG-I are key cytosolic pattern  
193 recognition receptors which recognize dsRNA (40), we performed RIP-seq analysis in DHX9  
194 depleted H446 cells that stably expressed either Flag-tagged MDA5 or RIG-I. Interestingly, we  
195 found that RNA levels in MDA5 pulldowns were significantly higher than RIG-I pulldowns (Fig.  
196 1J). More notably, sequencing results showed that dsRNA derived from LINEs and SINEs, which  
197 were also J2-enriched RNAs from sgDHX9 cells (Fig. 1H), were mainly bound to MDA5. This  
198 suggests that MDA5 might be a major contributor of dsRNA sensing pathway in DHX9 depleted  
199 cells (Fig. 1K).

200 To assess whether the helicase activity of DHX9 is required for suppressing dsRNAs in this  
201 model, we stably transduced H446 cells with Flag-tagged DHX9-WT or DHX9-K417R helicase  
202 dead mutant (Supplementary Fig. S1G) and performed RIP. Of note, we detected a significant  
203 increase of RNAs pulled down by DHX9-K417R helicase dead mutant, suggesting an impaired  
204 dsRNA unwinding capacity when compared to DHX9-WT (Fig. 1L) and supporting the idea that  
205 DHX9 helicase activity contributes to the suppression of dsRNA accumulation. Furthermore,  
206 sequencing RNAs from DHX9-K417R pulldowns demonstrated that SINEs and LINEs, which  
207 were enriched in sgDHX9 cells (Fig. 1H), can directly bind to DHX9 (Fig. 1M), further indicating  
208 these are targets of DHX9's helicase activity. Finally, heat map analysis of RIP-seq results

209 showed that the enrichment pattern of RNA species bound to DHX9-K417R was similar to  
210 MDA5, but not to RIG-I, further supporting the idea that dsRNAs which are sensed by MDA5 (>  
211 100bp) are the main targets of DHX9 (Fig. 1N). Taken together, these results demonstrate that  
212 DHX9 suppresses EREs-derived dsRNA accumulation by unwinding dsRNA in SCLC cells.

213

#### 214 **DHX9 depletion induces IFN response in SCLCs**

215 To investigate the biological impact of dsRNA accumulation in SCLC cells, we performed  
216 RNA sequencing (RNA-seq) on Scramble versus sgDHX9 SCLC cells. Consistently, Gene Set  
217 Enrichment Analysis (GSEA) revealed that DHX9 depletion induced the upregulation of gene  
218 expression pathways associated to immune and inflammatory responses and cytokine activity  
219 (Fig. 2A and B), and sgDHX9 cells showed increased expression of many Interferon Stimulated  
220 Genes (ISGs) by RNA-seq (Supplementary Fig. S2A). We validated by qRT-PCR that multiple  
221 ISGs (IFNB, CXCL10, CXCL11, CCL2), as well as nuclear factor kappa B (NF- $\kappa$ B)-responsive  
222 genes (TNFA, IL1B, RELB) were strongly induced by DHX9 loss, indicating the activation of an  
223 antiviral transcription program in response to DHX9 depletion (Fig. 2C; Supplementary Fig. S2B;  
224 Supplementary Table S2). sgDHX9 cells also showed increased levels of phospho (p-)IRF3 and  
225 p-TBK1 (Fig. 2D), markers of innate immunity able to activate a type I IFN response. Indeed, we  
226 were able to readily detect a significant increase in the secretion of IFN- $\beta$  into the culture medium  
227 after DHX9 depletion (Fig. 2E), as well as the secretion of multiple other cytokines and  
228 chemokines detected by Luminex multiplex assay (Fig. 2F; Supplementary Fig. S2C).

229 To further explore the potential impact of DHX9 loss on antitumor immunity, we analyzed cell  
230 surface expression of HLA-A, B, C on SCLC cells by flow cytometry, revealing a strong  
231 induction of these MHC class I molecules after DHX9 depletion (Fig. 2G; Supplementary Fig.  
232 S2D). Furthermore, DHX9 loss also induced cell surface PD-L1 expression (Fig. 2H;  
233 Supplementary Fig. S2E) which has been reported to be minimally expressed in more than 80% of  
234 SCLC tumors (41). Next, to evaluate the immunogenic capacity of dsRNAs produced after DHX9  
235 loss, we pulled down dsRNAs from DHX9 depleted cells using the J2 antibody and transfected  
236 these dsRNAs into recipient cells. Importantly, transfection of dsRNA isolated from DHX9  
237 depleted cells significantly activated IFNB expression in recipient cells, while digestion with  
238 RNase III (which cleaves dsRNA), completely canceled this effect (Fig. 2I), further suggesting  
239 that dsRNAs are responsible for the IFN response induced by DHX9 depletion. Together, these  
240 results indicate that DHX9 depletion activates dsRNA-sensing pathways and provoke the  
241 hypothesis that targeting DHX9 may provide unexplored strategies to activate antitumor immune  
242 pathways in SCLC.

243



## 244 **DHX9 depletion causes R-loop accumulation, DNA damage and cGAS-STING pathway** 245 **activation**

246 Intriguingly, we found that DHX9 depletion led not only to an increase in dsRNAs and an IFN  
247 response, but also to an upregulation of DNA damage-associated gene signatures and  
248 downregulation of cancer-associated pathways, when examined by analysis of RNA-seq data  
249 from DHX9 depleted SCLC cells (Fig. 2A and 3A). We validated by qRT-PCR in multiple DHX9  
250 depleted cells that genes involved in DNA damage were upregulated, while cancer-associated  
251 genes, such as genes related to DNA replication, were downregulated (Fig. 3B; Supplementary  
252 Fig. S3A). This finding suggests that conflicts in completing DNA replication in sgDHX9 cells  
253 might result in DNA damage. Indeed, IF and flow cytometry analysis showed that the DNA  
254 double-stranded breaks (DSBs) marker p-H2AX was strongly induced in multiple DHX9  
255 depleted cells (Fig. 3C and D; Supplementary Fig. S3B).

256 Previous studies reported that DHX9 is involved in unwinding R-loops, or DNA/RNA hybrid  
257 structures (42,43), and excessive R-loop formation can trigger genomic instability and replication  
258 stress by impairing replication fork progression and inducing DSBs (44,45), suggesting that  
259 aberrant R-loop accumulation might be a source of DNA damage in DHX9 depleted cells. To test  
260 this hypothesis, we first compared distribution and strength of R-loops (stained with S9.6  
261 DNA/RNA hybrid antibody) in Scramble versus sgDHX9 cells. Consistent with previous  
262 findings, we observed an increased accumulation of R-loop structures in sgDHX9 cells, which  
263 were efficiently degraded by RNase H treatment (Fig. 3E; Supplementary Fig. S3C). As we  
264 expected, loss of DHX9 also activated the DNA damage checkpoint pathway in H196, H82 and  
265 H1048 cells, as indicated by increased p-CHK1 and p-CHK2, and apoptosis, as indicated by  
266 cleaved PARP, as well as p-H2AX (Fig. 3F; Supplementary Fig. S3D). To test whether  
267 accumulation of R-loops is directly responsible for genomic instability and DNA damage, SCLC  
268 cells were transfected with a vector expressing RNase H1, which preferentially degrades the RNA  
269 portion of the R-loops. Exogenous RNase H1 expression suppressed the increase of p-CHK2,  
270 p-H2AX and cleaved PARP in sgDHX9 cells, supporting the idea that genomic instability and  
271 DNA damage in cells deficient for DHX9 was caused by accumulation of R-loops  
272 (Supplementary Fig. S3E). Next, we sought to determine the impact of DHX9 depletion on DNA  
273 replication stress and we performed the DNA fiber assay, which enables to analyze replication  
274 fork progression and processivity on single DNA molecules visualized by immunofluorescence  
275 (42,46). We found that the proportion of stalled forks significantly increased in DHX9 depleted  
276 cells (Fig. 3G), indicating that R-loop accumulation in cells deficient for DHX9 triggers  
277 replication stress which likely contributes to genomic instability.

278 Next, we asked whether helicase activity of DHX9 was required for unwinding of DNA/RNA  
279 hybrids in our model. Consistent with previous results, transfection of siDHX9-3'UTR decreased

280 cell growth of H446 cells, while expression of DHX9-WT, but not K417R helicase dead mutant,  
281 rescued the effects of DHX9 KD on cell viability (Supplementary Fig. S3F and S3G). Of note, we  
282 also found that DHX9-WT, but not K417R mutant, rescued the increase of DNA/RNA hybrids  
283 induced after DHX9 loss, suggesting that helicase activity of DHX9 is required to unwind  
284 DNA/RNA hybrid structures (Supplementary Fig. S3H).

285 The reduced expression of replication factors in sgDHX9 cells (Fig. 3B) raised the question of  
286 whether stalled replication forks might result from insufficient replication proteins. However, we  
287 found that exogenous expression of RNase H1, which resolves R-loops, decreased the number of  
288 stalled forks in sgDHX9 cells (Supplementary Fig. S3I). This further supports the idea that  
289 accumulation of R-loops contributes to fork stalling. In addition, because of key DNA repair  
290 genes were not upregulated in sgDHX9 cells, and to gain more insights into this mechanism, we  
291 reviewed RNA-seq data comparing sgDHX9 and Scr cells and found that senescence-related  
292 genes were upregulated in DHX9 depleted cells (Supplementary Fig. S3J and S3K). Consistent  
293 with this, secretion of cytokines related to aging/senescence (IL-1 $\beta$ , IL-6, IL-10, TNF- $\alpha$  and  
294 MCP-1) were strongly increased in sgDHX9 cells (Fig. 2F). As reported in previous studies  
295 (47,48), DNA damage might result in cellular senescence, and consequently DNA  
296 replication/repair genes might be downregulated. Based on these reports, DHX9 depleted cells  
297 might experience a senescence-like phenotype because of DNA damage, which can potentially  
298 contribute to the suppression of some key DNA repair genes.

299 Replication stress inducers including PARP and CHK1 inhibitors have been reported to activate  
300 innate immune responses through cGAS-STING pathway in SCLC cells (26). Thus, we next  
301 interrogated whether DHX9 loss-induced replication stress can contribute to the activation of  
302 cGAS-STING pathway and found that DHX9 depletion increased the number of cells with  
303 micronuclei that stained positive for cGAS and dsDNA, compared to Scramble cells (Fig. 3H). To  
304 measure cGAS activation, we then quantified by ELISA the levels of the second messenger,  
305 2'3'-cyclic GMP-AMP (cGAMP). This assay revealed that DHX9 depletion also elicited  
306 substantial increase in cGAMP production (Fig. 3I), suggesting an activation of the  
307 cGAS-STING pathway. Next, to examine the immunogenic capacity of cytosolic DNAs  
308 produced after DHX9 loss, we transfected cytoplasmic DNAs extracted from DHX9-depleted  
309 cells into recipient cells. Notably, transfection of cytoplasmic DNA isolated from DHX9 depleted  
310 cells significantly activated IFNB expression in recipient cells (Fig. 3J). Intriguingly, RNase H,  
311 which selectively degrades RNA strands in DNA/RNA hybrids, partially rescued IFNB induction  
312 caused by DNA transfection, while DNase I, which degrades DNA in the forms of dsDNA,  
313 ssDNA and DNA/RNA hybrids, almost completely canceled this effect. This suggests that  
314 cytoplasmic DNA/RNA hybrids, as well as dsDNAs accumulated after DHX9 depletion  
315 contribute to the induction of an IFN response in SCLC cells (Fig. 3J). Altogether, these data

316 indicate that the R-loops generated after DHX9 loss in SCLC cells promote DNA replication  
317 stress and DSBs, which likely contributes to the activation of an innate immune response.

318

### 319 **DHX9 loss triggers IFN signaling through dsRNA and dsDNA antiviral sensing pathways** 320 **in SCLC cells**

321 Based on the data above and that both innate immune responses and genomic instability can  
322 promote growth arrest and cell death, we next evaluated the effects of DHX9 depletion on SCLC  
323 cell proliferation and viability. We found a dramatic decrease in cell proliferation in all SCLC  
324 cells tested, including chemoresistant SCLC cells, as well as increased apoptosis (Fig. 4A and B;  
325 Supplementary Fig. S4A and S4B). Notably, DHX9 depletion had minimal effects on the  
326 proliferation and apoptosis of normal cells (Fig. 4C and D), and did not induce R-loop  
327 accumulation, nor increased the expression of p-CHK2, p-H2AX or cleaved PARP, supporting  
328 cancer cell-specific effects (Supplementary Fig. S4C and S4D). Most SCLCs lack functional  
329 TP53 and RB1, which are known to be drivers of genomic instability and replication stress  
330 (49-51), positioning DHX9 as a promising target and vulnerability to selectively accelerate  
331 replication stress-induced DNA damage in those tumors.

332 DHX9 depletion caused dsRNA and dsDNA accumulation in SCLC cells (Fig. 1G and  
333 Supplementary Fig. S1E; Fig. 3H), which could induce activation of dsRNA or dsDNA sensing  
334 pathways. Thus, to determine whether dsRNA or dsDNA sensing pathways are responsible for  
335 inducing antiviral innate immunity after DHX9 depletion, we performed CRISPR-mediated  
336 depletion of MAVS and STING combined with transfection of siCtrl or siDHX9. Notably,  
337 double-KO (dKO) of MAVS and STING was able to abrogate the induction of multiple ISGs  
338 (Fig. 4E) and IFN- $\beta$  protein secretion (Fig. 4F) observed after DHX9 depletion, as well as  
339 completely abrogate the phosphorylation of TBK1 and IRF3 induced by DHX9 loss (Fig. 4G). To  
340 systematically investigate which specific cytosolic nucleic-acid sensing pathways are activated  
341 by DHX9 loss, we depleted multiple nucleic acid sensors/mediators (cGAS, STING, MDA5,  
342 RIG-I, MAVS, PKR, TLR3 and TLR9), and tested IFNB and CXCL10 expression after DHX9  
343 loss (Supplementary Fig. S4E). Depletion of cGAS or STING strongly suppressed IFNB and  
344 CXCL10 induction upon DHX9 loss, and depletion of MDA5 or MAVS also partially rescued  
345 this phenotype, while depletion of other sensors had no significant effects. These results indicate  
346 that while the cGAS-STING pathway might have a major contribution to the IFN response,  
347 dsRNA sensing pathway (MDA5-MAVS) also plays a significant role. This further suggests that  
348 both cytoplasmic dsRNA and dsDNA generated upon DHX9 depletion contribute to downstream  
349 induction of antiviral and interferon pathways in SCLC cells.

350 To evaluate the contribution of cytoplasmic dsRNA/dsDNA sensing pathways to cell  
351 proliferation upon DHX9 loss, we depleted MAVS and STING individually, and as dKO, and

352 tested the effects of DHX9 loss on cell proliferation (Fig. 4H and Supplementary Fig. S4F).  
353 Co-depletion of MAVS and STING partially rescued cell growth defect, as well as depletion of  
354 each gene individually. Consistent with this, depletion of type I interferon signaling through  
355 IFNAR1 also partially rescued the growth defect caused by DHX9 loss (Supplementary Fig. S4G  
356 and S4H). Together, these data suggest a role of dsRNA and dsDNA sensing pathways on the  
357 antiviral immune response and cell death induced by DHX9 depletion. However, the observed  
358 partial rescue of cell proliferation also suggests that there may be redundancy in  
359 dsRNA/dsDNA-recognition pathways or that other pathways might contribute to DHX9  
360 depletion-induced cell death.

361

### 362 **CRISPR screen identifies modulators of sensitivity and resistance to DHX9 loss**

363 To interrogate the mechanisms by which DHX9 loss induces cell death in SCLC, we next  
364 performed a genome-wide, *in vitro* pooled CRISPR screen in SCLC cells to identify the genes  
365 whose deletion would rescue or increase the lethality observed following DHX9 depletion.  
366 Briefly, cells were transduced with the Brunello Human CRISPR Knockout Pooled Library (52)  
367 and selected in the presence of puromycin for efficient lentivirus transduction. Then, cells were  
368 transduced with either Scramble control or sgDHX9 vectors. Cells were further propagated, and  
369 genomic DNA was extracted to identify sgRNAs enriched and depleted in DHX9 depleted cells  
370 compared to control (Fig. 5A). This CRISPR screen identified multiple genes whose ablation  
371 resulted in resistance or sensitivity to DHX9 loss-induced lethality, and consequent enriched or  
372 depleted sgRNAs representation in sgDHX9 cells (Fig. 5B).

373 As expected, gene ontology (GO) analysis of the list of genes targeted by sgRNAs depleted in  
374 sgDHX9 cells revealed gene signatures related to cellular stress, DNA damage and DNA repair,  
375 indicating that loss of these genes increased the sensitivity of SCLC cells to DHX9  
376 loss-dependent cell death (Fig. 5C). Indeed, siRNA knockdown (KD) of AURKA, NMT1 and  
377 RHOQ genes, included in the top hits, accelerated cell death caused by siDHX9 (Supplementary  
378 Fig. S5A). Conversely, the screen also identified genes whose ablation resulted in resistance to  
379 DHX9 loss-induced lethality (sgRNAs enriched in DHX9 depleted population). Functional  
380 annotation of these genes revealed a striking enrichment for factors that are involved in RNA  
381 metabolic process, transcription, ribosome biogenesis and cell cycle checkpoint signaling (Fig.  
382 5D). One of the top sgRNAs enriched in DHX9 depleted cells were sgRNAs targeting CDK9  
383 (Fig. 5B), a kinase essential for transcriptional elongation (53). sgRNAs targeting CDK7, also  
384 involved in transcription elongation by phosphorylating CDK9, were also enriched in DHX9  
385 depleted population (Fig. 5B). Importantly, conflicts between transcription and DNA replication  
386 represent a significant cause of replication stress (45). These conflicts may result from the  
387 co-transcriptional occurrence of R-loops, which could impede the progression of DNA

388 replication forks (42,54). Interestingly, it has been previously reported that inhibition of CDK9  
389 decreased replication stress and DNA damage caused by R-loops, enabling DNA replication in  
390 cells treated with inhibitors or siRNAs against certain chromatin modifiers (55). Similarly,  
391 another study showed that RNA transcription is altered in the absence of p53, inducing increased  
392 replication stress and genomic instability that can be rescued by pharmacologic inhibition of  
393 transcription through CDK inhibitors (56). This raises the possibility that conflicts with  
394 transcription might cause replication stress when DHX9 is depleted. This may also explain why  
395 sgRNAs targeting CDK9 were able to rescue DHX9 depletion-induced lethality in our screen.  
396 Thus, ongoing transcription and perhaps the resulting R-loop formation might represent a  
397 prerequisite for impaired DNA replication upon DHX9 depletion leading to replication stress,  
398 DNA damage and ultimately cell death. Importantly, this might also explain why SCLC cells are  
399 particularly vulnerable to DHX9 deletion, as almost all SCLC tumors have loss of function  
400 mutations in TP53 and RB1 genes, which are linked with replication stress and genomic  
401 instability (49-51). We propose that a major source of replication stress in SCLC cells might arise  
402 from conflicts in transcription, as has been shown to occur in p53-deficient cells (56). Thus,  
403 therapeutic strategies that exacerbate this stress could selectively kill SCLC cells by replicative  
404 damage.

405 To validate the CRISPR screen results, we initially examined the protein levels of CDK9 and  
406 CDK7 in H82 cells employing the same sgRNAs used in the screen. We observed a reduction in  
407 both proteins, although these sgRNAs did not achieve a complete elimination of CDK9 and  
408 CDK7 protein levels (Supplementary Fig. S5B). Given the essential nature of CDK9 and CDK7,  
409 this partial reduction in their protein levels provides an explanation for the enrichment of  
410 sgRNAs targeting these essential genes in our screen. We also evaluated the impact of DHX9  
411 depletion on cell viability in sgCDK9 and sgCDK7 cells and confirmed that depletion of CDK9  
412 and CDK7 partially rescued the effects of DHX9 loss (Supplementary Fig. S5C). These findings  
413 align with the results of the CRISPR screen, where we observed an enrichment of sgRNAs  
414 targeting CDK9 and CDK7. Consistent with this, siRNAs targeting CDK9, as well as CDK7, also  
415 recovered cell growth of DHX9 KD H82 cells (Supplementary Fig. S5D). Importantly, we found  
416 that CDK9 inhibition with a potent and highly selective CDK9 inhibitor (BAY-1143572) rescued  
417 the decrease on cell proliferation and diminished the induction of p-CHK2, p-H2AX and  
418 cleaved-PARP observed after DHX9 depletion (Fig. 5E and F), although CDK9 inhibition  
419 decreased cell growth of FC1010 normal fibroblast cells (Supplementary Fig. S5E). Higher  
420 concentration of BAY-1143572 inhibited the SCLC cell growth as well (Supplementary Fig.  
421 S5F), consistent with previous reports (57). By performing the DNA fiber assay, we found that  
422 the proportion of stalled forks significantly increased in DHX9 depleted cells, and that CDK9  
423 inhibition greatly reduced the proportion of stalled forks both in sgDHX9 and control cells (Fig.

424 5G).

425 Given that CDK9 inhibition could affect transcription globally, which may indirectly contribute  
426 to the rescuing effects, we performed dot blot experiments using the S9.6 antibody to directly  
427 evaluate R-loop accumulation in DHX9 depleted cells after CDK9 inhibition. Consistent with  
428 previous results, we observed a significant increase of R-loops in sgDHX9 cells, which was  
429 partially rescued by CDK9 inhibition (Supplementary Fig. S5G). Furthermore, we directly  
430 measured gene-specific R-loop level using qDRIP (Quantitative differential DNA/RNA Immuno  
431 Precipitation) (Supplementary Figs. S5H-S5P) (58). Of note, CDK9 inhibitor treatment alleviated  
432 R-loop build-up at multiple promoter regions, including Gadd45b, RhoB (direct DHX9-targeted  
433 genes) (59), and ThumpD2 (Supplementary Figs. S5N-S5P). Additionally, we confirmed that  
434 CDK9 inhibition had no significant effects on the expression levels of key nucleic acid sensors or  
435 mediators, excluding any potential impact of CDK9 inhibition in pathways involved in  
436 dsRNA/dsDNA sensing (Supplementary Fig. S5Q). These findings indicate that a major source of  
437 replication stress in SCLC cells arises from transcription-associated damage, which is further  
438 induced by DHX9 depletion (Fig. 5H).

439 Together, these results illuminate a novel mechanism of DHX9 loss-induced cell death in  
440 cancer cells and position DHX9 as a promising therapeutic target for SCLC and other tumor types  
441 where genomic instability and replication stress contribute to pathology.

442

#### 443 **DHX9 depletion decreases tumor growth, induces immune cell infiltration and enhances** 444 **response to immune checkpoint blockade therapy**

445 The induction of immune transcriptional programs by DHX9 loss (Figs. 2A-C) suggests the  
446 hypothesis that such immune signaling may also impact the tumor microenvironment and  
447 provoke antitumor immune responses. To test this hypothesis, we generated RPP cells (a murine  
448 SCLC cell line generated by triple knockout of Tp53, Rb1, Rbl2 genes (24,60)) stably expressing  
449 shRNA targeting either control (shCtrl) or Dhx9 (shDhx9) under control of a Tet-inducible  
450 promoter, into the flanks of C57BL/6 mice (Fig. 6A). When tumors became palpable, the mice  
451 were fed with doxycycline water to induce DHX9 KD (Fig. 6B and C). We found that DHX9 KD  
452 significantly decreased tumor volume and weight (Fig. 6D; Supplementary Fig. S6A), while body  
453 weight of mice was not affected by the treatment (Supplementary Fig. S6B). To better understand  
454 the *in vivo* immune consequences of DHX9 depletion in SCLC, we evaluated tumor infiltration of  
455 immune cells by flow cytometry analysis and observed a striking increase of immune cells  
456 expressing NK-1.1, CD11b and F4/80 (Fig. 6E). In addition, intratumoral cytotoxic CD8<sup>+</sup> T cells  
457 were significantly increased in shDhx9 tumors, indicating a functional immune response, while  
458 CD4<sup>+</sup> T cells did not change significantly (Fig. 6F; Supplementary Fig. S6C; Supplementary  
459 Table S6). Immunohistochemical (IHC) analysis also confirmed enhanced infiltration of CD8<sup>+</sup> T

460 cells, as well as F4/80<sup>+</sup> macrophages in DHX9 depleted tumors (Fig. 6G). Thus, these data  
461 demonstrates that DHX9 KD enhances immunogenicity *in vivo* potentially bypassing a major  
462 pathway of cancer cell immune evasion. To further assess whether immune cells are responsible  
463 for the reduced growth of DHX9 depleted tumors, we first evaluated the effects of DHX9  
464 depletion in immunodeficient (NSG) mice using the same murine SCLC cell line (RPP cells) to  
465 replicate the same experimental conditions. We found that while DHX9 depletion decreased  
466 tumor volume in NSG mice (Supplementary Fig. S6D), this effect on tumor growth was smaller  
467 when compared to the effects of DHX9 depletion observed in immunocompetent mice (Fig. 6D).  
468 These results further suggest that both DNA damage and immune infiltration induced by DHX9  
469 depletion contribute to the reduced tumor growth. Furthermore, given that CD8<sup>+</sup> T cells and NK  
470 cells were significantly increased in DHX9 depleted tumors (Fig. 6E and F), we then performed  
471 same *in vivo* experiment as in Fig. 6D and tested the effects of CD8<sup>+</sup> T cell depletion and NK cell  
472 depletion using CD8a antibody and NK1.1 antibody, respectively. While we found that CD8<sup>+</sup> T  
473 cell depletion slightly rescued the decrease in tumor growth observed after DHX9 loss, the  
474 observed partial rescue also suggests that other immune cell types might contribute to the reduced  
475 tumor growth observed in DHX9 depleted tumors (Supplementary Fig. S6E). Together, these  
476 results suggest that immune cells, as well as intracellular replication stress, contribute to the  
477 reduced growth of DHX9 KD tumors.

478 As DHX9 loss induced IFN response and increased intratumoral infiltration of cytotoxic CD8<sup>+</sup>  
479 T cells in SCLC tumors, we next sought to determine whether DHX9 depletion potentiates  
480 ICB-based immunotherapy in the SCLC syngeneic model. To accomplish this, we treated  
481 immunocompetent C57BL/6 bearing RPP cells expressing DOX-inducible shCtrl or shDhx9 with  
482 either anti-PD-1 or isotype IgG control antibodies. We excluded anti-CTLA-4 antibodies because  
483 based on multiple clinical trials there is currently no role for anti-CTLA-4 antibodies in the  
484 treatment of SCLC (61-63). Notably, while control RPP tumors were not very sensitive to  
485 PD-1/PD-L1 blockade, consistent with a previous report (26), DHX9 depletion dramatically  
486 enhanced the sensitivity of RPP tumors to anti-PD-1 therapy, resulting in increased mouse  
487 survival (Fig. 6H and I). To validate our findings in a second *in vivo* model, we generated KP3  
488 cells (mouse SCLC cell line derived from the RP GEMM model) (64,65), stably expressing  
489 DOX-inducible shCtrl or shDhx9 and engrafted them into the flanks of immunocompetent  
490 recipient mice (Supplementary Fig. S6F). Similarly, DHX9 loss also enhanced the sensitivity of  
491 RP tumors to anti-PD-1 therapy, resulting in increased mouse survival (Supplementary Fig. S6G  
492 and S6H). Again, we observed a striking increase of CD8<sup>+</sup> T cells in shDhx9 tumors  
493 (Supplementary Fig. S6I and S6J). Taken together, these data suggest that DHX9 loss in SCLC  
494 tumors induces a robust antitumor immunity which may ultimately lead to improved ICB  
495 treatment outcomes in immunologically cold tumors.

496

497 **DHX9 is negatively correlated with immune signatures and associated with poor clinical**  
498 **outcomes in cancer patient datasets**

499 To investigate whether DHX9 is associated with human tumorigenesis, we tested DHX9  
500 protein expression by immunohistochemistry (IHC) in a human SCLC tissue microarray (TMA),  
501 including 40 SCLC tumor samples and normal lung controls (Fig. 7A). Consistent with the public  
502 transcriptomic data (Fig. 1D), SCLC tumors exhibited higher staining intensity of DHX9 than  
503 normal counterparts (Fig. 7B). Notably, DHX9 expression increased in higher tumor stages,  
504 supporting the association of high DHX9 expression and poor patient prognosis in SCLC patients.

505 We next interrogated transcriptomic data from a human SCLC dataset (51) to determine  
506 whether DHX9 expression is associated with the tumor immune microenvironment. GSEA  
507 analysis revealed that DHX9 expression inversely correlated with gene signatures involved in  
508 IFN-alpha response, as well as inflammatory response (Fig. 7C), confirming our results from *in*  
509 *vitro* and *in vivo* models. Indeed, many of the IFN-stimulated genes and NF-kB-responsive genes  
510 were tended to be highly expressed in DHX9<sup>low</sup> group (Supplementary Fig. S7A). We also  
511 interrogated TCGA to explore the broader relevance of DHX9 across human lung cancers and GO  
512 analysis revealed that gene signatures involved in IFN-related pathways were strongly  
513 upregulated in DHX9 low-expressing lung cancer tumors when compared to DHX9  
514 high-expressing tumors (Fig. 7D), suggesting that DHX9 is a crucial repressor of tumor-intrinsic  
515 innate immunity in human lung tumors. DHX9 expression was also inversely correlated with  
516 DNA damage response, consistent with activation of apoptosis and DNA damage checkpoint  
517 pathway in sgDHX9 cells *in vitro* (Fig. 3F). In addition, pan-cancer analysis exhibited a strong  
518 negative correlation between DHX9 expression and gene signatures of inflammatory response  
519 and innate immune response in a variety of tumor types (Fig. 7E). Consistent with this, GSEA  
520 analysis of pan-cancer RNA-seq data also showed an upregulation of interferon-alpha response  
521 and inflammatory response in DHX9<sup>low</sup> tumors (Supplementary Fig. S7B).

522 To anticipate the clinical relevance of targeting DHX9 for immunotherapy, we created a  
523 DHX9-depleted gene signature (Supplementary Table S3), including genes which were  
524 upregulated in sgDHX9 cells based on RNA-seq analysis and related to the two most prominent  
525 features of DHX9 depleted cells: DNA damage response and immune response. Given that this  
526 signature is expected to be upregulated when DHX9 is inhibited in cancer cells, we wanted to  
527 evaluate its clinical relevance in immunotherapy settings. Thus, we assessed the potential  
528 predictive value of DHX9 inhibition across public datasets of patients treated with  
529 anti-PD-1-based or anti-CTLA-4-based ICB therapy (66-68). Notably, we found that high levels  
530 of the DHX9-depleted gene signature were positively associated with ICB response across most  
531 of the datasets, suggesting that DHX9 inhibition may sensitize cancers to immunotherapy (Fig.



532 7F). In addition, the estimated immune-score of the tumor microenvironment in DHX9<sup>low</sup> tumors  
533 tended to be higher than DHX9<sup>high</sup> tumors (Supplementary Fig. S7C). Thus, these data provide  
534 evidence that DHX9 inhibition could sensitize tumors to ICB therapies, including  
535 immunologically cold tumors such as SCLC (Fig. 7G).  
536

537 **Discussion**

538 Induction of innate immune responses in tumor cells has been gathering attention as a  
539 promising strategy to enhance ICB therapy response (10,11,26), especially in immunologically  
540 cold tumors. Here, we demonstrate that the RNA helicase DHX9 functions as a repressor of  
541 innate immune signaling and replication stress in cancer cells through unwinding of dsRNA and  
542 R-loop structures.

543 Our study revealed that depletion of DHX9 induces immunogenic dsRNAs, causing tumor  
544 cell-intrinsic antiviral signaling, and alters transcription and DNA replication in cancer cells to  
545 induce formation of R-loops, compromising genome stability and cell viability. Notably,  
546 triggering these tumor-intrinsic events greatly improves ICB treatment outcomes in  
547 immunologically cold tumors, such as SCLC. While prior studies have shown the potential of  
548 DHX9 to unwind dsRNA (38,69), DNA/RNA hybrids (31,70) and other more complex nucleic  
549 acid structures (32), our findings strongly suggest that dsRNAs and R-loops derived from DHX9  
550 depletion directly contribute to induction of innate immune responses and replication stress in  
551 cancer cells, highlighting its potential as novel target to enhance antitumor immunity and boost  
552 cancer immunotherapy. Recently, a study reported by Crossley and colleagues demonstrated that  
553 DNA/RNA hybrids derived from R-loops are sensed by cGAS and TLR3 and activate an innate  
554 immune response and apoptosis (71), which is further supported by the data presented here,  
555 suggesting that R-loop-inducing therapies might be a therapeutic strategy to effectively enhance  
556 antitumor immunity while concurrently induce DNA damage and compromise cell viability in  
557 cancer cells.

558 Almost all SCLCs exhibit inactivation of TP53 and RB1, both of which are key regulators of  
559 DNA damage and cell cycle checkpoint (49-51). Intriguingly, while genomic instability in SCLC  
560 is among the highest in all the cancer types (72), the tumor microenvironment tends to be immune  
561 desert (16), which might explain the reason why SCLCs are relatively unresponsive to ICB  
562 therapies and remains as a recalcitrant disease (20). Thus, an urgent need exists to identify novel  
563 targets to improve outcomes of SCLC patients, considered the most lethal type of lung cancer.  
564 Increasing evidence has now emerged indicating that targeting components of the DNA Damage  
565 Response (DDR) pathway, including PARP, CHK1 or WEE1, might be an effective strategy with  
566 significant antitumor effects in SCLC preclinical models (12,13,25). Importantly, recent studies  
567 showed that DDR inhibitors potentiates ICB therapies in SCLC preclinical models by evoking  
568 beneficial IFN responses in the tumor microenvironment through accumulating cytosolic DNA  
569 and activating cGAS-STING and STAT1 pathways (26,27). Intriguingly, we found that DHX9  
570 depletion in SCLC cells triggers innate immune signaling and DNA damage through dsRNA and  
571 R-loop production, at least partially generated from various EREs and genomic instability,

572 representing a more robust viral mimicry-inducing factor and a vulnerability preferentially in  
573 cancer cells under replication stress.

574 A major reason explaining the poor response of cold tumors to immunotherapy is the lack of an  
575 immunogenic tumor microenvironment, often linked to decreased CD8<sup>+</sup> T cell abundance and a  
576 defective IFN signaling (73). Our data in immunocompetent SCLC mouse models indicate that  
577 the tumor-intrinsic effects of DHX9 depletion not only induced a significant decrease in tumor  
578 growth, but also led to the recruitment of multiple immune cells into the TMA, including CD8<sup>+</sup> T  
579 cells, dramatically sensitizing SCLC tumors to anti-PD-1 immunotherapy. These findings  
580 strongly suggest that targeting DHX9 could potentially convert immunologically cold tumors to  
581 hot, while concurrently promote cancer cell death.

582 Results from this study support efforts aimed at designing DHX9 inhibitors to exploit its  
583 therapeutic potential as anti-cancer therapy and to improve responsiveness to immunotherapy in  
584 immunologically cold tumors. While DHX9 is reported to be essential during embryonic  
585 development, additional studies using conditional knockdown systems showed that reduced  
586 levels of DHX9 in adult mice did not cause any deleterious effects at the organismal level,  
587 although DHX9 loss was lethal to tumor cells (74). Consistent with this data, our findings indicate  
588 that DHX9 depletion has minimal or no effects on the proliferation of normal cells, which also  
589 emphasize the contribution of intrinsic replication stress to DHX9 loss-related cell death in SCLC  
590 cells and suggest that targeting DHX9 might be an effective and realistic therapeutic strategy to  
591 treat cancers.

592 Given that DHX9 is broadly expressed and plays a central role in diverse cell homeostasis  
593 processes, potential consequences of direct DHX9 inhibition need to be carefully evaluated in  
594 future studies. A recent study reported that DHX9 is required for a productive CD8<sup>+</sup> T cell  
595 response against viral infection, protecting T cell from apoptosis and regulating genes that are  
596 necessary for effector T cell differentiation independent of its nuclear sensor role (75). Based on  
597 these observations, it might be argued that systemic treatment with DHX9 inhibitors could restrict  
598 the antitumor activity of certain immune cells. However, we and others have shown that DHX9 is  
599 overexpressed in certain cancers, including SCLC (Fig. 1D) (76-78), and that rapidly dividing  
600 tumor cells which are under replication stress are heavily vulnerable to DHX9 depletion  
601 compared to normal cells, highlighting the potential for a therapeutic window in which tumor  
602 growth control could be achieved with limited toxicity. Importantly, the fact that DHX9 depletion  
603 not only impact cancer cell survival but also potentiates antitumor immune responses to ICB  
604 therapy in SCLC models, might open a new range of therapeutic possibilities that will expand the  
605 breadth and depth of response to cancer immunotherapies. Nevertheless, further research should  
606 be conducted to fully evaluate the systemic consequences of DHX9 inhibition.

607 In summary, our study identified DHX9 as a novel vulnerability in immunologically cold  
608 tumors, especially in those whose genome is instable, such as SCLC. We show that DHX9 is a  
609 crucial suppressor of dsRNA and R-loop accumulation, and the genetic perturbation of DHX9  
610 leads to innate immune response activation, as well as DNA replication stress and DNA damage.  
611 Moreover, we found that these tumor-intrinsic effects can turn cold tumors into hot, dramatically  
612 enhancing ICB responsiveness and highlighting DHX9 as a potential novel target to boost cancer  
613 immunotherapy in immunologically cold tumors.  
614  
615

## 616 **Methods**

### 617 **Cell lines and cell culture**

618 The human SCLC cell lines NCI-H69, NCI-H69AR, NCI-H841, SHP-77, NCI-H187,  
619 NCI-H345, NCI-H524, NCI-H1048 and NCI-H82 were obtained from the laboratory of Dr. Joan  
620 Albanell and were authenticated following short tandem repeat (STR) genotyping. RPP SCLC  
621 mouse cell line was obtained from the laboratory of Dr. Matthew Oser. KP3 (RP) SCLC mouse  
622 cell line was obtained from the laboratory of Dr. Julien Sage. RPE cells were obtained from the  
623 laboratory of Dr. Johnathan R. Whetstone, FC1010 primary fibroblast cells were isolated in the  
624 FCCC tissue culture facility (from Dr. Hossein Borghaei), and were authenticated following STR  
625 genotyping. NCI-H196, NCI-H446, NCI-H1436, NCI-H2081, Colo668, NCI-H1694, NCI-H841,  
626 DMS 114 and HEK293T cells were obtained from the American Type Culture Collection and  
627 used for all experiments before reaching 10 passages. NCI-H69M was established from  
628 NCI-H69, as previously reported (79). All cells were routinely tested for mycoplasma and found  
629 to be free of contamination.

630 H69, H69M, H69AR, H82, H446, H196, SHP-77, H187, H345, H524, H1436, H2081,  
631 Colo668, H1694, H841, H1048 and DMS 114 were cultured in RPMI-1640 containing 10% fetal  
632 bovine serum (FBS, Hyclone), 2.5 g/L Glucose and 1X penicillin/streptomycin (10,000 U/mL;  
633 Thermo Fisher Scientific). HEK293T was maintained in Dulbecco's Modified Eagles Medium  
634 (DMEM) containing 10% FBS and 1X penicillin/streptomycin. RPP and KP3 mouse cell lines  
635 were cultured in RPMI-1640 containing 10% FBS, 1X penicillin/streptomycin, and HITES (1X  
636 insulin-transferrin-selenium, 10 nM  $\beta$ -estradiol, and 10 nM hydrocortisone). RPE was cultured in  
637 DMEM/F-12, 10% FBS, 2.5 mM L-glutamine, 15 mM HEPES, 0.5 mM Sodium pyruvate and  
638 0.01 mg/ml hygromycin. FC1010 was cultured in RPMI-1640 with 15% FBS, 2 mM  
639 L-glutamine, 1 mM Sodium pyruvate and 1X penicillin/streptomycin. All cells were maintained  
640 in a humidified incubator with 5% CO<sub>2</sub> at 37°C. Subtypes of SCLC cell lines are summarized in  
641 Supplementary Table S4.

642

### 643 **CRISPR-Cas9 gene editing vectors**

644 Target sequences of DHX9, MAVS, STING, IFNAR1, DNA/RNA sensors and RNA helicases  
645 (for screen) for CRISPR interference were designed using the single-guide RNA (sgRNA)  
646 designer (<http://portals.broadinstitute.org/gpp/public/analysis-tools/sgrna-design>). Sequences  
647 of sgRNA for human DHX9 were 5'-GGGGTAGAATCTGATACCGA-3' (sgDHX9), and  
648 5'-CAAAACATTATACTGGCATG-3' (sgDHX9 #2). sgRNA sequences of human MAVS and  
649 STING were 5'-ACTGGAGCAGATGATAGGCT-3' and  
650 5'-GGTACCGGGCAGCTACTGG-3', respectively. sgRNA sequence of human IFNAR1 was  
651 5'-GTACATTGTATAAAGACCAC-3'. sgRNA sequences of RNA helicase genes and

652 DNA/RNA sensor genes are listed in Supplementary Table S1. sgRNA from the Gecko library v2  
653 was used as a dummy sgRNA (5'-ATCGTTTCCGCTTAACGGCG-3') for Scramble control  
654 (Scr). LentiCRISPR v2 vectors were cloned as previously described (80,81). Lentiviral plasmids  
655 were transduced into HEK293T cells along with pMD2.G and psPAX2 using X-treme Gene 9  
656 DNA Transfection Reagent (Roche; no. XTG9-RO) according to the manufacturer's instructions.  
657 The 48-hour supernatant of transduced HEK293T cells was collected and filtered with a 0.45 µm  
658 filter.

659

### 660 **Transduction of SCLC cells with lentiviral vectors**

661 Culture supernatant from HEK293T cells containing virus particles was applied to SCLC cell  
662 lines, with 8 µg/mL polybrene (Santa Cruz Biotechnology; no. sc-134220). Cells were  
663 centrifuged with virus at 2000 rpm at 37°C for 2 hours. The cells were incubated at 37°C in 5%  
664 CO<sub>2</sub> for 24 hours, and then the media were replaced with complete RPMI-1640. Virus-infected  
665 cells were selected for 48 hours using 1.0 µg/mL puromycin (Gibco) or 5.0 µg/mL blasticidin  
666 (Gibco), from 48 hours post-infection.

667

### 668 **siRNA transfection**

669 DHX9 siRNAs (no. s4020, s4021) were purchased from Thermo Fisher Scientific, with s4021  
670 used in most experiments. The siRNA targeting the 3'UTR of DHX9 was purchased from  
671 horizon (no. A-009950-16-0005). A nonspecific control siRNA duplex (siCtrl) was purchased  
672 from Thermo Fisher Scientific (Silencer Select Negative Control No. 1 siRNA, no. 4390844).  
673 Other siRNAs used in this study included AURKA (no. s197), NMT1 (no. s9602), RHOQ (no.  
674 s23825), CDK9 (no. s2835) and CDK7 (no. s2829) (Thermo Fisher Scientific). siRNAs were  
675 transfected using Lipofectamine RNAiMAX Transfection Reagent (Thermo Fisher Scientific;  
676 no. 13778500) according to the manufacturer's instructions.

677

### 678 **Immunohistochemical (IHC) staining**

679 Mouse tumor tissues were collected and fixed in 10% neutral buffered formalin for 24 hours,  
680 dehydrated, and embedded in paraffin. Hematoxylin and eosin (H&E)-stained sections were used  
681 for morphologic evaluation purposes and 5-µm unstained sections for IHC studies.

682 IHC staining was carried out on a VENTANA Discovery XT automated staining instrument  
683 (Ventana Medical Systems) using VENTANA reagents according to the manufacturer's  
684 instructions. Briefly, slides were de-paraffinized using EZ Prep solution (no. 950-102) for  
685 16 minutes at 72 °C. Epitope retrieval was accomplished with CC1 solution (EDTA, pH 9.0.; no.  
686 950-224) at high temperature (eg, 95–100 °C) for 32 minutes. Rabbit primary antibodies:  
687 anti-mouse CD8 (1:50, Cell Signaling Technology; no. 98941), anti-mouse CD45 (1:50, Cell

688 Signaling Technology; no. 70257) and F4/80 (1:800, Cell Signaling Technology; no. 70076)  
689 tittered with a TBS antibody diluent into user fillable dispensers for use on the automated stainer.  
690 Immune complex was detected using the Ventana OmniMap anti-Rabbit detection kit (no.  
691 760-4311) and developed using the VENTANA ChromMap DAB detection kit (no. 760-159)  
692 according to the manufacturer's instructions. Slides were then counterstained with hematoxylin II  
693 (no. 790-2208) for 8 minutes, followed by Bluing reagent (no. 760-2037) for 4 minutes.

694 The slides were then dehydrated with ethanol series, cleared in xylene, and mounted. As a  
695 negative control, the primary antibody was replaced with normal rabbit IgG to confirm absence of  
696 specific staining.

697

### 698 **Quantitative Image analysis**

699 Immunostained slides were scanned using an Aperio ScanScope CS 5 slide scanner (Aperio).  
700 Scanned images were then viewed with Aperio's image viewer software (ImageScope, version  
701 11.1.2.760, Aperio). Selected regions of interest were outlined manually by a pathologist. The  
702 positive percentage score for CD8, CD45 and F4/80 was quantified using the Aperio V9  
703 algorithm.

704

### 705 **Immunoblotting**

706 Protein was extracted from cell lines with Pierce RIPA Buffer (Thermo Fisher Scientific; no.  
707 89900) and quantified by Pierce BCA Protein Assay Kit (Thermo Fisher Scientific; no. 23225).  
708 Protein extracts were subjected to polyacrylamide gel electrophoresis using the 4%-12%  
709 NuPAGE gel system (Invitrogen), transferred to PVDF membranes (Millipore). Transferred  
710 protein was immunoblotted using antibodies against TBK1 (no. 3013), S172 pTBK1 (no. 5483),  
711 IRF3 (no. 4302), S396 pIRF3 (no. 4947), S345 pCHK1 (no. 2348), T68 pCHK2 (no. 2197),  
712 S139 pH2AX (no. 9718), Cleaved PARP (no. 5625), STING (no. 13647), MAVS (no. 3993),  
713 CDK9 (no. 2316), CDK7 (no. 2090),  $\beta$ -actin (no. 3700) (Cell Signaling Technology), mouse  
714 DHX9 (no. ab26271), IFNAR1 (no. ab124764), V5 tag (no. ab27671) (Abcam) and human  
715 DHX9 (no. sc-137232) (Santa Cruz Biotechnology) after blocking with LICOR Blocking Buffer  
716 (LICOR; no. 927-60001).

717 Secondary antibodies were purchased from LICOR Biosciences: IRDye 800CW Goat  
718 anti-Mouse IgG (H+L) (no. 926-32210) and IRDye 800CW Goat anti-Rabbit IgG (H+L) (no.  
719 926-32211). LICOR Antibody Diluent (LICOR; no. 927-65001) was used to dilute primary and  
720 secondary antibodies. Phosho-specific antibodies were diluted in CanGet Signal  
721 Immunoreaction Enhancer Solutions (TOYOBO; no. NKB-101) 1 (for primary) and 2 (for  
722 secondary). Imaging of blots was performed using the LICOR Odyssey system.

723

724 **Immunocytochemistry**

725 Cells were plated on BioCoat Culture Slide (Corning; no. 354630) after trypsinization, and  
726 incubated overnight. To detect expression of proteins in nuclei and micronuclei, cells were fixed  
727 with 4% paraformaldehyde (PFA) for 10 minutes and permeabilized with 0.5% Triton X-100 for  
728 15 minutes. After blocking with MAXblock Blocking Medium (Active Motif; no. 15252) for 1  
729 hour at 37°C, cells were stained overnight at 4°C with primary antibodies and for 1 hour at room  
730 temperature with secondary antibodies. Coverslips were mounted with ProLong Gold Antifade  
731 reagent with DAPI (Invitrogen; no. P36935), and immunofluorescent visualization of nuclei was  
732 counterstained with DAPI in the reagent. Immunofluorescence was detected using Leica SP8  
733 confocal microscope and analyzed with ImageJ software. Antibody against dsRNA (J2; 1:200,  
734 no. 10010200) was purchased from SCICONS, S139 pH2AX (1:1000, no. 9718) and cGAS  
735 (1:100, no. 79978) were purchased from Cell Signaling Technology, dsDNA antibody (1:100, no.  
736 ab27156) was from Abcam. For RNase III treatment, cells were treated with 20 U/mL of RNase  
737 III for 30 minutes at 37°C before fixation.

738 To detect DNA/RNA hybrid, cells were fixed with ice-cold, 100% methanol for 20 minutes at  
739 -20°C, and permeabilized with 0.5% Triton X-100 for 15 minutes. Cells were incubated with  
740 antibody against DNA/RNA hybrid (Sigma-Aldrich; no. MABE1095, clone S9.6) at 1:50 dilution  
741 overnight at 4°C, followed by secondary donkey anti-mouse IgG (H+L) conjugated with Alexa  
742 Fluor 594 at 1:500 dilution for 1 hour at room temperature. For RNase H treatment, cells were  
743 incubated with 120 U RNase H (Takara Bio; no. 2150A) for 4 hours in RNase H buffer (40 mM  
744 Tris-HCl pH8.0, 4 mM MgCl<sub>2</sub>, 1 mM dithiothreitol, 4% glycerol, and 0.003% BSA) before  
745 immunocytochemistry assay.

746

747 **ELISA**

748 IFN- $\beta$  ELISA (R&D Systems; no. DIFNB0) and 2',3'-Cyclic GAMP (cGAMP) ELISA  
749 (Arbor Assays; no. K067-H1) kits were used according to the manufacturer's instructions.  
750 Conditioned media from cells cultured for 72 hours after seeding (for IFN- $\beta$ ), and cell lysates  
751 (for cGAMP) were collected and analyzed. For cells treated with siRNAs, 72 hours-culture  
752 conditioned media from the cells were collected at Day 6 after transfection.

753 For cytokine array assay, Proteome Profiler Human Cytokine Array Kit (R&D Systems; no.  
754 ARY005B) was used according to the manufacturer's instructions. Conditioned media was  
755 collected 72 hours after seeding the cells.

756

757 **Flow cytometry analysis**

758 For detecting proteins on cell membrane, collected cells were washed with PBS and stained  
759 with anti-PD-L1 (BioLegend; no. 329718, isotype control: no. 400232), anti-HLA-A, B, C



760 (Biolegend; no. 311410, isotype control: no. 400220) antibodies diluted with PBS containing  
761 2% FBS at 2  $\mu\text{g}/\text{mL}$ . Stained cells were analyzed on a BD LSR II Flow Cytometer, fluorescence  
762 levels were compared with isotype control antibodies. Data were analyzed using the FlowJo  
763 software (TreeStar). Dead cells were excluded by staining with PI or Zombie NIR Fixable  
764 Viability Kit (BioLegend; no. 423106).

765 For intracellular flow cytometry, collected cells were fixed with 4% formaldehyde in PBS  
766 and permeabilized with 0.1% Triton X-100 in PBS. The cells were then incubated with primary  
767 antibodies, followed by secondary antibodies. Primary antibody against dsRNA (J2; 1:200, no.  
768 10010200) was purchased from SCICONS, S139 pH2AX (1:1000, no. 9718) was from Cell  
769 Signaling Technology. Isotype controls, normal mouse IgG2a (no. ab18413) and rabbit IgG (no.  
770 ab172730) were purchased from Abcam. Secondary donkey anti-mouse IgG (H+L) conjugated  
771 with Alexa Fluor 488 (no. A32766) and donkey anti-rabbit IgG (H+L) conjugated with Alexa  
772 Fluor 488 (no. A32790) were purchased from Thermo Fisher Scientific. Dead cells were  
773 excluded by pre-fixation staining with Zombie NIR Fixable Viability Kit.

774

#### 775 **Murine SCLC GEMM, cell line derivation, and tumor implantation studies**

776 The RPP-631 (RPP) SCLC mouse cell lines were established in the laboratory of Dr. Matthew  
777 G. Oser (Dana-Farber Cancer Institute, Boston, MA, USA), which were originally derived from  
778 SCLC tumors that were generated in LSL-Cas9 C57BL/6 mice that were intratracheally injected  
779 with AAV that encode Cre-recombinase and sgRNAs targeting Trp53, Rb1, and Rbl2 (RPP)  
780 genes (60). Histopathology of the tumor from which the cell lines were derived showed small cell  
781 lung cancer.

782 To generate the syngeneic mouse tumor model,  $8.0 \times 10^6$  RPP cells, which stably expressing  
783 SMARTvector tet-inducible Dhx9 shRNA (horizon; no. V3SM11253) or control shRNA  
784 (horizon; no. VSC11652), were subcutaneously implanted into the flank of C57BL/6 mice or  
785 NSG mice, after mixing with Matrigel (Corning; no. 354234) at 1:1 ratio. To generate RP tumors,  
786  $1.0 \times 10^6$  KP3 cells (a kind gift from Dr. Julien Sage) were subcutaneously implanted into the  
787 flank of B6129SF1 mice, after mixing with Matrigel at 1:1 ratio. Doxycycline water (5% sucrose  
788 with 2 mg/mL of doxycycline; Sigma) was provided to all the groups to induce knockdown of  
789 Dhx9 gene, once palpable tumor formation was confirmed. The doxycycline water was changed  
790 every other day. Tumor size was measured every 2-3 days by digital caliper. Tumor volumes were  
791 calculated using the formula:  $\text{volume} = (\text{length} \times \text{width}^2)/2$ . Both Female and male C57BL/6 mice  
792 (Jackson Laboratories) of 6-8 weeks old were used for the transplantation studies.

793

#### 794 **Antibody treatment, tumor collection and survival analysis**

795 Mice were euthanized with CO<sub>2</sub> and their tumors were quickly extracted, washed in PBS, and  
796 minced using a sterilized razor blade. For tumor IHC staining of CD8, CD45 and F4/80, and flow  
797 cytometry analysis of infiltrated immune cells, all mice were euthanized on day 32  
798 post-inoculation of RPP cells. Collected tumor tissues were fixed in 10% phosphate-buffered  
799 formaldehyde for IHC, and were processed for flow cytometry analysis using the Tumor  
800 Dissociation Kit, mouse (Miltenyi; no. 130-096-730) and GentleMACS Dissociator (Miltenyi;  
801 no. 130-093-235), according to manufacturer's instructions, followed by washing and filtering  
802 with a 70 µm cell strainer.

803 For combination treatments, mice were administered 200 µg rat IgG2a isotype control  
804 (BioXCell; no. BP0089) or anti-PD-1 antibody (BioXCell; no. BP0146) via i.p. injection on days  
805 17, 19, 21, 23 and 25 post-inoculation of RPP cells. Doxycycline water was provided once  
806 palpable tumor formation was confirmed, to induce knockdown of Dhx9 gene. Tumor size was  
807 measured every 2-3 days by digital caliper, and mouse survival was monitored with tumor  
808 volume exceeding 1000 mm<sup>3</sup>, weight loss >15%, and decreasing behavioral conditions  
809 considered as endpoints.

810 For depletion of CD8 T cells or NK cells, C57BL/6 mice were treated with 10 mg/kg anti-CD8a  
811 antibody (BioXCell; no. BP0061) or anti-NK1.1 antibody (BioXCell; no. BP0036), twice per  
812 week.

813

#### 814 **Quantitative PCR with reverse transcription (qRT-PCR)**

815 Total RNAs were extracted using the RNeasy Mini Kit (Qiagen; no. 74106) according to the  
816 manufacturer's instructions. 1 µg of extracted RNA was used to generate cDNA with the  
817 SuperScript III First-Strand Synthesis SuperMix for RT-qPCR kit (Thermo Fisher Scientific;  
818 no. 18080-044). qRT-PCR of the indicated genes (Supplementary Table S2) was performed  
819 using Power SYBR Green PCR Master Mix (Applied Biosystems; no. 4367659) and the  
820 Applied Biosystems QuantStudio 6 Pro Real-Time PCR System and software. The relative  
821 expression was normalized with the expression of the housekeeping genes 36B4 (for human  
822 cells) or Actb (for mouse cells), and analyzed with the  $-\Delta\Delta C_t$  relative quantification method.

823

#### 824 **RNA-seq**

825 Total RNAs were extracted and purified using the RNeasy Mini Kit (Qiagen; no. 74106) from  
826 NCI-H196, NCI-H446 and NCI-H82 cells, which were infected with lentivirus containing  
827 Scramble or sgDHX9 vector, at day 7 post-selection. Using a 2100 Bioanalyzer RNA 6000 Nano  
828 assay (Agilent), quality of RNA was assessed. RNA concentration was measured using a Qubit  
829 2.0 Fluorometer (Life Technologies). Illumina sequencing libraries were constructed using the

830 NEBNext Ultra II Directional RNA Library Prep Kit for Illumina (NEB), and sequenced on  
831 Illumina NovaSeq 6000 by pair-end sequencing with a read length of  $2 \times 150$  bp, by Novogene.

832 Expression levels for each gene were quantified from the sequencing data using Kallisto (82).  
833 The data were then summarized using the tximport package (ver. 1.18.0) of R software (ver.  
834 4.0.3) and RStudio (RStudio), and scaledTPM counts were used for further analysis as expression  
835 values. GSEA was performed to identify gene signatures which are upregulated and  
836 downregulated in sgDHX9 cells compared to Scramble, or DHX9<sup>low</sup> tumors compared to  
837 DHX9<sup>high</sup> tumors (for data from database).

838

### 839 **RNA immunoprecipitation and sequencing (RIP-seq)**

840 Scramble or sgDHX9 H446 cells ( $2.0 \times 10^7$ ) were harvested, and RNA immunoprecipitation  
841 (RIP) was conducted using a Magna RIP RNA-Binding Protein Immunoprecipitation kit  
842 (Sigma-Aldrich; no. 17-700), according to the manufacturer's instructions. Briefly, cell pellets  
843 were lysed in RIP lysis buffer, followed by incubation with RIP buffer containing magnetic beads  
844 conjugated with J2 (SCICONS; no. 10010200) or isotype control (abcam; no. ab18413) antibody  
845 at 4°C overnight. Samples were then incubated with proteinase K, and immunoprecipitated RNAs  
846 were recovered by phenol:chloroform:isoamyl alcohol purification. RNA was quantified using a  
847 QuantiFluor RNA System (Promega; no. E3310) and assessed for quality with the 2100  
848 Bioanalyzer RNA 6000 Nano assay (Agilent) before library generation. Ribosomal RNA (rRNA)  
849 was removed using NEBNext rRNA Depletion Kit v2 (NEB; no. E7400L) according to the  
850 manufacturer's instructions. For pulling down of MDA5 and RIG-I bound RNA, we transfected  
851 pcDNA3-Flag-MDA5 and pcDNA3-Flag-RIG-I expression vector, respectively, to DHX9  
852 depleted cells 2 days before collecting RNA. Anti-Flag (DYKDDDDK)-tag antibody (Invitrogen;  
853 no. MA1-91878) was used for IP. For pulling down of DHX9 bound RNA, we prepared  
854 pCDH-3xFlag-DHX9-K417R expressing H446 cells and performed IP using anti-Flag  
855 (DYKDDDDK)-tag antibody.

856 Illumina sequencing libraries were prepared by Novogene, with the NEBNext Ultra II RNA  
857 Library Prep Kit for Illumina (NEB), according to the manufacturer's instructions. Libraries were  
858 analyzed for insert size distribution using the 2100 Bioanalyzer RNA 6000 Nano assay (Agilent).  
859 Libraries were quantified using the Qubit 2.0 Fluorometer (Life Technologies), and sequenced on  
860 Illumina NovaSeq 6000 by pair-end sequencing with a read length of  $2 \times 150$  bp, by Novogene.

861 For analysis of RE expression from RIP-seq data, the trimmed FASTQ reads by TrimGalore  
862 (version 0.6.4) were mapped against *H. sapiens* UCSC hg19 using the Bowtie 2 (version 2.3.5)  
863 alignment software (83). The counts of RE were calculated by *RepEnrich2* (84) using default  
864 settings, and were normalized by one million reads as CPM (counts per million). In this  
865 software, reads mapping uniquely to the genome are assigned to subfamilies of repetitive

866 elements based on their degree of overlap to “*RepeatMasker*” annotated genomic instances of  
867 each repetitive element subfamily. On the other hand, reads mapping to multiple locations are  
868 separately mapped to repetitive element assemblies – referred to as repetitive element  
869 pseudogenomes. By combining the counts from uniquely mapping reads and multi-mapping  
870 reads “*RepEnrich2*” keeps track of all repetitive elements that every read aligns to and  
871 systematically estimates enrichment from all mapping reads. The heatmap was visualized using  
872 the “*ggplot2*” package of R software (version 4.0.5).

873

#### 874 **RIP-qRT-PCR**

875 Scramble or sgDHX9 H446 cells ( $5.0 \times 10^6$ ) were harvested, and cytoplasmic fractions were  
876 extracted using the Nuclear Extract Kit (Active Motif; no. 40010), according to the  
877 manufacturer’s instructions. To isolate RNA, an equal volume of 70% ethanol was added to the  
878 cytoplasmic fractions, and then, according to the manufacturer’s instructions, purification was  
879 performed using the RNeasy Plus Mini Kit (QIAGEN; no. 74106). The total RNA was dissolved  
880 with 38  $\mu$ L RNase-free H<sub>2</sub>O. Then 2  $\mu$ L total RNA was used as input and the remainder divided  
881 into 2 tubes. 2  $\mu$ g of J2 antibody (SCICONS; no. 10010200) and mouse control IgG2a (abcam;  
882 no. ab18413) were conjugated to 20  $\mu$ L protein G agarose (Millipore; no. 16-266) per pulldown,  
883 by rotation overnight at 4°C. To digest single stranded RNA, 1  $\mu$ L of RNase A (Sigma-Aldrich;  
884 no. R6513) was added to each tube and then mixed with 1 mL IP buffer (50 mM Tris-HCl [pH  
885 7.4], 125 mM NaCl, 1 mM EDTA, 0.1% Triton X-100). The RNA samples were incubated with  
886 antibody-conjugated protein G agarose beads overnight at 4°C. Beads were washed with IP  
887 buffer three times, and then incubated in 50  $\mu$ L proteinase K digestion solution (1X TE, 100  
888 mM NaCl, 1% SDS, and 1  $\mu$ L of 20 mg/mL Proteinase K solution (Thermo Fisher Scientific;  
889 no. AM2546)) for 20 min at 45°C to isolate RNA. After centrifugation, 50  $\mu$ L of the supernatant  
890 was added to 300  $\mu$ L Buffer RLT Plus from the RNeasy Plus Mini Kit (QIAGEN; no. 74106) to  
891 purify RNA. The final product containing dsRNA was denatured for 5 min at 95°C, followed by  
892 reverse transcription using qScript cDNA SuperMix (Quantabio; no. 95048), which contains  
893 both random primers and oligo(dT) primer. qRT-PCR was performed using the primers listed in  
894 Supplementary Table S2, by Applied Biosystems QuantStudio 6 Pro Real-Time PCR System  
895 and software.

896

#### 897 **DNA fiber assay**

898 Cells were pulsed-labeled with 25  $\mu$ M IdU (Sigma-Aldrich; no. I7125) for the first 30  
899 minutes, followed by 250  $\mu$ M CIdU (Sigma-Aldrich; no. C6891) for 30 minutes. The cells were  
900 trypsinized and resuspended in PBS, then diluted to the concentration of  $1.0 \times 10^5$ - $1.0 \times 10^6$   
901 cells/mL. At the end of an APS-coated glass slide (Matsunami; no. SUAPS1190), 2  $\mu$ L of cell

902 suspension was placed. After air drying for 8 minutes, 7  $\mu$ L of fiber lysis solution (200 mM  
903 Tris-HCl [pH 7.5], 50 mM EDTA, 0.5% SDS) was pipetted on top of the cell suspension and  
904 mixed gently. Cell lysis proceeded for 5 minutes. The slides were tilted at 15° to allow the DNA  
905 spread down to the bottom of the slide. Slides were air-dried for 15 minutes and fixed in  
906 methanol/acetic acid (3:1). After washing with distilled water, DNA was denatured in 2.5 M  
907 HCl for 80 minutes. The slides were washed with PBS three times, and blocked in 5% BSA in  
908 PBS for 1 hour. After blocking, the slides were incubated with primary antibodies, anti-IdU  
909 (BD; no. 347580) and anti-CldU (Abcam; no. ab6326) and followed by secondary antibodies,  
910 donkey anti-mouse IgG (H+L) conjugated with Alexa Fluor 488 (Thermo Fisher Scientific; no.  
911 A32766) and donkey anti-rat IgG (H+L) conjugated with Alexa Fluor 594 (Thermo Fisher  
912 Scientific; no. A21209).

913

#### 914 **Proliferation assay**

915 Cells were seeded in 12-well plates at low density (2,500-10,000 cells/well), cultured in  
916 complete RPMI-1640 medium, in a humidified incubator with 5% CO<sub>2</sub> at 37°C. After 2, 4, 6 and  
917 8 days, cells were harvested and counted.

918

#### 919 **Transfection of cytoplasmic dsRNA/DNA**

920 Cytoplasmic fraction was extracted from DHX9 depleted cells ( $4.0 \times 10^6$ ) using the Nuclear  
921 Extract Kit (Active Motif; no. 40010), according to the manufacturer's instructions.  
922 Cytoplasmic DNA was extracted using the Gel Extraction Kit (QIAGEN; no. 28704) after  
923 treatment of RNase A/T1 Mix (Thermo Fisher Scientific; no. EN0551). To isolate RNA, an equal  
924 volume of 70% ethanol was added to the cytoplasmic fractions, and purification was performed  
925 using the RNeasy Plus Mini Kit (QIAGEN; no. 74106). Pulldown of dsRNA was performed as  
926 detailed in the "RIP-qRT-PCR" section.

927 For the cytoplasmic DNA re-transfection assay, extracted cytoplasmic DNA was digested with  
928 1  $\mu$ L DNase I (Thermo Fisher Scientific; no. EN0521), 1  $\mu$ L RNase H (NEB; no. M0523S) or 1  
929  $\mu$ L H<sub>2</sub>O (mock) in 10  $\mu$ L reaction mixture for 60 minutes at 37°C prior to re-transfection into  
930 H196 cells with Lipofectamine 3000 (Thermo Fisher Scientific; no. L3000001). For cytoplasmic  
931 dsRNA re-transfection, purified dsRNA was digested with 1  $\mu$ L RNase III (Thermo Fisher  
932 Scientific; no. AM2290) or 1  $\mu$ L H<sub>2</sub>O (mock) in 5  $\mu$ L reaction mixture for 60 minutes at 37°C  
933 prior to re-transfection. After 24 hours, RNA was isolated using the RNeasy Plus Mini Kit.

934

#### 935 **DHX9 expression vectors**

936 The wild-type and helicase dead mutant (K417R) human DHX9 cDNAs were cloned into  
937 pCDH-3xFLAG-GFP-puroR vector (a kind gift from Dr. Lu Chen) with the AscI/PacI sites,

938 generating pCDH-3xFLAG-DHX9 (WT/K417R)-puroR. For rescue experiments, siRNA  
939 targeting DHX9-3'UTR was transfected to knockdown only endogenous DHX9.

940

#### 941 **R-loop detection by dot blot**

942 For R-loop (DNA/RNA hybrid) detection by dot blot, DNA samples were prepared using DRIP  
943 protocol, as previously reported (85). Briefly, cells were lysed in 1.6 mL TE buffer, containing 50  
944  $\mu$ L of 20% SDS and 5  $\mu$ L of 20 mg/mL proteinase K at 37°C overnight. Extracted DNA was  
945 phase separated using phenol/chloroform/isoamyl alcohol (25:24:1), precipitated with ethanol  
946 and resuspended in TE buffer. Then, purified DNA was digested using cocktail of restriction  
947 enzymes (HindIII, SspI, EcoRI, BsrGI and XbaI; 30 U each), treated with RNase A (10  $\mu$ g/mL)  
948 and RNase III (2U) and again purified by phenol/chloroform/isoamyl alcohol (25:24:1). DNA  
949 were spotted on a nitrocellulose membrane, blocked with LICOR Blocking Buffer and incubated  
950 with antibody against DNA/RNA hybrid (Sigma-Aldrich; no. MABE1095, clone S9.6) dsDNA  
951 (Abcam; no. ab27156). Secondary antibody; IRDye 800CW Goat anti-Mouse IgG (H+L)  
952 (LICOR; no. 926-32210) was used to detect the signal. purchased from LICOR Biosciences:  
953 and IRDye 800CW Goat anti-Rabbit IgG (H+L) (no. 926-32211). Imaging of blots was  
954 performed using the LICOR Odyssey system.

955

#### 956 **Generation and characterization of synthetic Spike-in R-loop**

957 Synthetic R-loop spike-in was generated according to (86). Briefly, E. coli genomic DNA  
958 was isolated by phenol-chloroform extraction. A 320 bp of DNA was PCR amplified with  
959 L286F (T7-promoter bearing) and L286R (Supplementary Table S2) and purified using DNA  
960 Clean & Concentrator-5 (Zymo Research; no. D4014). *In vitro* transcription (IVT) reactions  
961 were carried out at 37°C for 1 hour with the HiScribe® T7 High Yield RNA Synthesis Kit  
962 (NEB; no. E2040S) with 200ng of template DNA. RNA was purified using the Direct-zol RNA  
963 Miniprep kit (Zymo Research; no. R2052). RNA was checked by running a 7% UREA-PAGE  
964 gel. Complementary L286 ssDNA was synthesized by IDT (Supplementary Table S2), and the  
965 DNA/RNA hybrid was reconstituted with a molar ratio of 1:5 in the NEB Buffer 2.1. The  
966 reconstituted hybrid is fractionated in 1.8% agarose gel, from which the RNase H sensitive  
967 species was excised and eluted following a gel-crushing method (87). The purified R-loop was  
968 quantitated by agarose gel electrophoresis followed by SYBR green II staining. R-loop is  
969 further characterized by an R-loop EMSA assay containing 0.55 nM of R-loop and S9.6  
970 antibody (0.11 and 0.55 nM). The reaction was incubated at 37°C for 30 minutes and fractioned  
971 in a 5% native PAGE gel visualized by SYBR green II staining.

972

#### 973 **Quantitative DNA-RNA Immunoprecipitation-qPCR with Spike-Ins (qDRIP-qPCR)**

974 qDRIP was performed as per the method detailed by (86). Briefly, H82 cells were pelleted at  
975 500 x g for 5 minutes, followed by resuspension in 4 mL of DPBS and a gently layered 3 mL of  
976 Ficoll Paque Plus (Cytiva; no. 17144003). This was centrifuged at 400 x g for 40 minutes at  
977 room temperature to separate live cells. 750,000 trypan-blue-negative cells per experimental  
978 condition were resuspended in 1.6 mL of TE buffer, to which 5  $\mu$ L of a 16.7 fM of synthetic  
979 E.coli DNA/RNA hybrid L286 was added as spike-in control (see below). Cells were incubated  
980 in 50  $\mu$ L of 20% SDS and 5  $\mu$ L of Proteinase K (20 mg/ml, Thermo Fisher Scientific; no.  
981 EO0491) at 37°C for 3 hours, followed by phenol-chloroform extraction and ethanol  
982 precipitation. The DNA was then sonicated to an average fragment length of 300 bp using the  
983 QSonica 800R3 (no. Q800R3-110) at 40% Amplitude, 15 seconds ON or OFF alternating for a  
984 total of 7 minutes ON time. The resulting fragment distribution was analyzed using High  
985 Sensitivity TapeStation D1000 screentape (Agilent; no. 5067-5584). Immunoprecipitation was  
986 performed with the S9.6 antibody (Kerafast; no. Kf-Ab01137-23.0) and DynaGreen Protein  
987 A/G Magnetic Beads (Thermo Fisher Scientific; no. 80106G). RNase H treatment (NEB; no.  
988 M0297S) was carried out at 37°C overnight. The qPCR reactions were then conducted using 2X  
989 qRT-PCR Brilliant III SYBR Master Mix (Agilent; no. 600886) on the QuantStudio 6 Flex  
990 Real-Time PCR System (Thermo Fisher Scientific; 4485691). The results of these reactions  
991 were analyzed using R version 4.3.1.

992

### 993 **Viability assay**

994 Cells were plated in 96-well plates at low density (2,000-8,000 cells/well), cultured in complete  
995 RPMI-1640 medium, in a humidified incubator with 5% CO<sub>2</sub> at 37°C for 96 hours. Luminescent  
996 values of CellTiter-Glo Cell Viability assay (Promega; no. G7571) were obtained by the  
997 CLARIOstar Plus Microplate Reader and software (BMG Labtech).

998

### 999 **CRISPR screen and analysis**

1000 On day 0 (day of infection),  $\sim 7.0 \times 10^7$  ( $\sim 1000$  cells/sgRNA) H82 cells, which stably express  
1001 Cas9, were resuspended in complete media with 10% FBS, 8  $\mu$ g/mL polybrene at a concentration  
1002 of  $1.0 \times 10^6$  cells/mL in 50 mL conical tubes, and the Human Brunello CRISPR knockout pooled  
1003 library was added at an MOI of 0.3. The cells were then distributed onto low-adherence 6-well  
1004 plates at a density of  $2.0 \times 10^6$  cells per well, and the plates were centrifuged at 2000 rpm for 2  
1005 hours. The following day (day 1), the virus was removed by changing media, and the cells were  
1006 transferred to low-adherence 10 cm plates at a concentration of  $0.4 \times 10^6$  cells/mL. On day 4, the  
1007 cells were plated in fresh media in the presence of 1  $\mu$ g/mL puromycin and were selected for 72  
1008 hours.

1009 Following completion of puromycin selection (day 7), resistant cells were replated with fresh  
1010 media and grown in complete media until day 13. On day 13,  $2.5 \times 10^7$  cells were mixed with  
1011 lentivirus containing Scramble or sgDHX9, with 8  $\mu\text{g}/\text{mL}$  polybrene. The cells were then  
1012 distributed onto low-adherence 6-well plates at a density of  $2.0 \times 10^6$  cells per well, and the plates  
1013 were centrifuged at 2000 rpm for 2 hours. The following day (day 14), the virus was washed  
1014 away, and the cells were transferred to low-adherence 10 cm plates. Until Day 23, the cells were  
1015 grown in complete media, keeping a minimum of  $2.5 \times 10^7$  cells per group. The screen was  
1016 performed in 3 biological replicates.

1017 After completion of the screen, genomic DNA (gDNA) was isolated using Blood & Cell  
1018 Culture DNA Midi Kit (Qiagen; no. 13343) according to the manufacturer's protocol. To attach  
1019 sequencing adaptors and barcode samples, PCR of gDNA was performed using Ex Taq DNA  
1020 Polymerase (TaKara; no. RR001), as previously described (52). Samples were purified with  
1021 Agencourt AMPure XP SPRI beads according to the manufacturer's instructions (Beckman  
1022 Coulter; no. A63880). Purified DNA samples were sequenced on a Nextseq2000 (Illumina). The  
1023 sgRNA read count and hits calling were analyzed by MAGeCK v0.5.7 algorithm (88). Each gene  
1024 symbol of enriched or depleted sgRNAs in DHX9-loss population was mapped to Gene Ontology  
1025 resources (<http://www.geneontology.org/>) to rank gene ontology terms.

1026 Human Brunello CRISPR knockout pooled library (52) was a gift from Drs. David Root and  
1027 John Doench (Addgene; no. 73178).

1028

### 1029 **Pan-cancer analysis of TCGA dataset**

1030 TCGA pan-cancer gene expression with patient annotation datasets were retrieved from the  
1031 Genomic Data Commons (GDC) of the National Cancer Institute  
1032 (<https://gdc.cancer.gov/about-data/publications/pancanatlas>). Signature scores of different tumor  
1033 types were calculated in GSVA using the "z-score" method (89). Spearman correlation and  
1034 multiple testing corrections were done in R software (ver. 4.0.3).

1035

### 1036 **Data availability**

1037 The RNA-seq data is deposited in the GEO repository (Accession Number; GSE244103). We  
1038 also registered raw data of RIP-seq experiments in the GEO repository (Accession Number;  
1039 GSE244104 (J2), GSE247217 (Flag)). Data generated from the CRISPR screen are provided in  
1040 Supplementary Table S5. All other data and materials can be requested from the corresponding  
1041 author.

1042

### 1043 **Statistical analyses**



1044 All graphs depict mean  $\pm$  SEM unless otherwise indicated. Tests for differences between two  
1045 groups were performed using two-tailed unpaired Student's t-test or Mann-Whitney test.  
1046 Two-way analysis of variance (ANOVA) was performed where applicable using Tukey's  
1047 multiple comparison test. Values of  $p < 0.01$ – $0.05$  (\*),  $p < 0.001$ – $0.01$  (\*\*),  $p < 0.001$ – $0.0001$   
1048 (\*\*\*), or  $p < 0.0001$  (\*\*\*\*) were considered significant. GraphPad Prism7 was used for statistical  
1049 analysis of experiments, data processing, and presentation.

1050

### 1051 **Study approval**

1052 All animal experiments were performed under protocols approved by Institutional Animal Care  
1053 and Use Committee at FCCC.

1054

1055 **Author Contributions**

1056 Conception and design: T. Murayama, I. Cañadas

1057 Development of methodology: T. Murayama, J. Nakayama, X. Jiang, AD. Morris, K.Q. Cai, R.

1058 Prasad, X. Ma, A. Efimov, N. Belani, ER. Gerstein, K.S. Campbell, L. Chen, Y. Yang, I. Cañadas

1059 Acquisition of data: T. Murayama, J. Nakayama, AD. Morris, K.Q. Cai, Y. Tan, J.W. Kim, I.

1060 Cañadas

1061 Analysis and interpretation of data: T. Murayama, J. Nakayama, K.Q. Cai, K. Miyata, AD.

1062 Morris, Y. Tan, Y. Zhou, J.W. Kim, R. Maruyama, L. Chen, Y. Yang, S. Balachandran, I.

1063 Cañadas

1064 Writing, review, and/or revision of the manuscript: T. Murayama, N. Belani, S. Balachandran, I.

1065 Cañadas

1066 Project administration: I. Cañadas

1067 All authors read the manuscript and provided feedback on the manuscript before submission.

1068

1069 **Acknowledgements**

1070 The authors thank Dr. David A. Barbie (Dana-Farber Cancer Institute, Boston, MA, USA) for

1071 critically reading the manuscript. The GEMM-derived SCLC cell line RPP was kindly provided

1072 by Dr. Matthew G. Oser (Dana-Farber Cancer Institute, Boston, MA, USA). The GEMM-derived

1073 SCLC cell line KP3 (RP) was kindly provided by Dr. Julien Sage (Stanford University, Stanford,

1074 CA,USA). The authors thank Mengmeng Li (Fox Chase Cancer Center, Philadelphia, PA, USA)

1075 for statistical consulting.

1076

1077

1078 **References**

1079

- 1080 1. Demaria O, Cornen S, Daeron M, Morel Y, Medzhitov R, Vivier E. Harnessing innate  
 1081 immunity in cancer therapy. *Nature* **2019**;574(7776):45-56 doi  
 1082 10.1038/s41586-019-1593-5.
- 1083 2. Ribas A, Dummer R, Puzanov I, VanderWalde A, Andtbacka RHI, Michielin O, *et al.*  
 1084 Oncolytic Virotherapy Promotes Intratumoral T Cell Infiltration and Improves  
 1085 Anti-PD-1 Immunotherapy. *Cell* **2017**;170(6):1109-19 e10 doi  
 1086 10.1016/j.cell.2017.08.027.
- 1087 3. Ishizuka JJ, Manguso RT, Cheruiyot CK, Bi K, Panda A, Iracheta-Vellve A, *et al.*  
 1088 Loss of ADAR1 in tumours overcomes resistance to immune checkpoint blockade.  
 1089 *Nature* **2019**;565(7737):43-8 doi 10.1038/s41586-018-0768-9.
- 1090 4. Ribas A, Medina T, Kummar S, Amin A, Kalbasi A, Drabick JJ, *et al.* SD-101 in  
 1091 Combination with Pembrolizumab in Advanced Melanoma: Results of a Phase Ib,  
 1092 Multicenter Study. *Cancer Discov* **2018**;8(10):1250-7 doi  
 1093 10.1158/2159-8290.CD-18-0280.
- 1094 5. Zhang J, Huang D, Saw PE, Song E. Turning cold tumors hot: from molecular  
 1095 mechanisms to clinical applications. *Trends Immunol* **2022**;43(7):523-45 doi  
 1096 10.1016/j.it.2022.04.010.
- 1097 6. Mehdipour P, Marhon SA, Ettayebi I, Chakravarthy A, Hosseini A, Wang Y, *et al.*  
 1098 Epigenetic therapy induces transcription of inverted SINEs and ADAR1 dependency.  
 1099 *Nature* **2020**;588(7836):169-73 doi 10.1038/s41586-020-2844-1.
- 1100 7. Sheng W, LaFleur MW, Nguyen TH, Chen S, Chakravarthy A, Conway JR, *et al.*  
 1101 LSD1 Ablation Stimulates Anti-tumor Immunity and Enables Checkpoint Blockade.  
 1102 *Cell* **2018**;174(3):549-63 e19 doi 10.1016/j.cell.2018.05.052.
- 1103 8. Shen JZ, Qiu Z, Wu Q, Finlay D, Garcia G, Sun D, *et al.* FBXO44 promotes DNA  
 1104 replication-coupled repetitive element silencing in cancer cells. *Cell*  
 1105 **2021**;184(2):352-69 e23 doi 10.1016/j.cell.2020.11.042.
- 1106 9. Canadas I, Thummalapalli R, Kim JW, Kitajima S, Jenkins RW, Christensen CL, *et al.*  
 1107 Tumor innate immunity primed by specific interferon-stimulated endogenous  
 1108 retroviruses. *Nat Med* **2018**;24(8):1143-50 doi 10.1038/s41591-018-0116-5.
- 1109 10. Chiappinelli KB, Strissel PL, Desrichard A, Li H, Henke C, Akman B, *et al.*  
 1110 Inhibiting DNA Methylation Causes an Interferon Response in Cancer via dsRNA  
 1111 Including Endogenous Retroviruses. *Cell* **2015**;162(5):974-86 doi  
 1112 10.1016/j.cell.2015.07.011.
- 1113 11. Roulois D, Loo Yau H, Singhanian R, Wang Y, Danesh A, Shen SY, *et al.*

- 1114 DNA-Demethylating Agents Target Colorectal Cancer Cells by Inducing Viral  
1115 Mimicry by Endogenous Transcripts. *Cell* **2015**;162(5):961-73 doi  
1116 10.1016/j.cell.2015.07.056.
- 1117 12. Byers LA, Wang J, Nilsson MB, Fujimoto J, Saintigny P, Yordy J, *et al.* Proteomic  
1118 profiling identifies dysregulated pathways in small cell lung cancer and novel  
1119 therapeutic targets including PARP1. *Cancer Discov* **2012**;2(9):798-811 doi  
1120 10.1158/2159-8290.CD-12-0112.
- 1121 13. Sen T, Tong P, Stewart CA, Cristea S, Valliani A, Shames DS, *et al.* CHK1 Inhibition  
1122 in Small-Cell Lung Cancer Produces Single-Agent Activity in Biomarker-Defined  
1123 Disease Subsets and Combination Activity with Cisplatin or Olaparib. *Cancer Res*  
1124 **2017**;77(14):3870-84 doi 10.1158/0008-5472.CAN-16-3409.
- 1125 14. Von Hoff DD, Rasco DW, Heath EI, Munster PN, Schellens JHM, Isambert N, *et al.*  
1126 Phase I Study of CC-486 Alone and in Combination with Carboplatin or  
1127 nab-Paclitaxel in Patients with Relapsed or Refractory Solid Tumors. *Clin Cancer*  
1128 *Res* **2018**;24(17):4072-80 doi 10.1158/1078-0432.CCR-17-3716.
- 1129 15. DiNardo CD, Jonas BA, Pullarkat V, Thirman MJ, Garcia JS, Wei AH, *et al.*  
1130 Azacitidine and Venetoclax in Previously Untreated Acute Myeloid Leukemia. *N*  
1131 *Engl J Med* **2020**;383(7):617-29 doi 10.1056/NEJMoa2012971.
- 1132 16. Hegde PS, Chen DS. Top 10 Challenges in Cancer Immunotherapy. *Immunity*  
1133 **2020**;52(1):17-35 doi 10.1016/j.immuni.2019.12.011.
- 1134 17. Rudin CM, Brambilla E, Faivre-Finn C, Sage J. Small-cell lung cancer. *Nat Rev Dis*  
1135 *Primers* **2021**;7(1):3 doi 10.1038/s41572-020-00235-0.
- 1136 18. Chalmers ZR, Connelly CF, Fabrizio D, Gay L, Ali SM, Ennis R, *et al.* Analysis of  
1137 100,000 human cancer genomes reveals the landscape of tumor mutational burden.  
1138 *Genome Med* **2017**;9(1):34 doi 10.1186/s13073-017-0424-2.
- 1139 19. Antonia SJ, López-Martin JA, Bendell J, Ott PA, Taylor M, Eder JP, *et al.*  
1140 Nivolumab alone and nivolumab plus ipilimumab in recurrent small-cell lung cancer  
1141 (CheckMate 032): a multicentre, open-label, phase 1/2 trial. *The Lancet Oncology*  
1142 **2016**;17(7):883-95 doi 10.1016/s1470-2045(16)30098-5.
- 1143 20. Horn L, Mansfield AS, Szczesna A, Havel L, Krzakowski M, Hochmair MJ, *et al.*  
1144 First-Line Atezolizumab plus Chemotherapy in Extensive-Stage Small-Cell Lung  
1145 Cancer. *N Engl J Med* **2018**;379(23):2220-9 doi 10.1056/NEJMoa1809064.
- 1146 21. Liu SV, Reck M, Mansfield AS, Mok T, Scherpereel A, Reinmuth N, *et al.* Updated  
1147 Overall Survival and PD-L1 Subgroup Analysis of Patients With Extensive-Stage  
1148 Small-Cell Lung Cancer Treated With Atezolizumab, Carboplatin, and Etoposide  
1149 (IMpower133). *Journal of clinical oncology : official journal of the American Society*

- 1150 of Clinical Oncology **2021**;39(6):619-30 doi 10.1200/JCO.20.01055.
- 1151 22. Gadgeel SM, Pennell NA, Fidler MJ, Halmos B, Bonomi P, Stevenson J, *et al.* Phase  
1152 II Study of Maintenance Pembrolizumab in Patients with Extensive-Stage Small  
1153 Cell Lung Cancer (SCLC). *J Thorac Oncol* **2018**;13(9):1393-9 doi  
1154 10.1016/j.jtho.2018.05.002.
- 1155 23. Gay CM, Stewart CA, Park EM, Diao L, Groves SM, Heeke S, *et al.* Patterns of  
1156 transcription factor programs and immune pathway activation define four major  
1157 subtypes of SCLC with distinct therapeutic vulnerabilities. *Cancer Cell*  
1158 **2021**;39(3):346-60 e7 doi 10.1016/j.ccell.2020.12.014.
- 1159 24. Mahadevan NR, Knelson EH, Wolff JO, Vajdi A, Saigi M, Campisi M, *et al.* Intrinsic  
1160 Immunogenicity of Small Cell Lung Carcinoma Revealed by Its Cellular Plasticity.  
1161 *Cancer Discov* **2021**;11(8):1952-69 doi 10.1158/2159-8290.CD-20-0913.
- 1162 25. Sen T, Tong P, Diao L, Li L, Fan Y, Hoff J, *et al.* Targeting AXL and mTOR Pathway  
1163 Overcomes Primary and Acquired Resistance to WEE1 Inhibition in Small-Cell  
1164 Lung Cancer. *Clin Cancer Res* **2017**;23(20):6239-53 doi  
1165 10.1158/1078-0432.CCR-17-1284.
- 1166 26. Sen T, Rodriguez BL, Chen L, Corte CMD, Morikawa N, Fujimoto J, *et al.* Targeting  
1167 DNA Damage Response Promotes Antitumor Immunity through STING-Mediated  
1168 T-cell Activation in Small Cell Lung Cancer. *Cancer Discov* **2019**;9(5):646-61 doi  
1169 10.1158/2159-8290.CD-18-1020.
- 1170 27. Taniguchi H, Caeser R, Chavan SS, Zhan YA, Chow A, Manoj P, *et al.* WEE1  
1171 inhibition enhances the antitumor immune response to PD-L1 blockade by the  
1172 concomitant activation of STING and STAT1 pathways in SCLC. *Cell Rep*  
1173 **2022**;39(7):110814 doi 10.1016/j.celrep.2022.110814.
- 1174 28. Jiao S, Xia W, Yamaguchi H, Wei Y, Chen MK, Hsu JM, *et al.* PARP Inhibitor  
1175 Upregulates PD-L1 Expression and Enhances Cancer-Associated  
1176 Immunosuppression. *Clin Cancer Res* **2017**;23(14):3711-20 doi  
1177 10.1158/1078-0432.CCR-16-3215.
- 1178 29. Shen J, Zhao W, Ju Z, Wang L, Peng Y, Labrie M, *et al.* PARPi Triggers the  
1179 STING-Dependent Immune Response and Enhances the Therapeutic Efficacy of  
1180 Immune Checkpoint Blockade Independent of BRCAness. *Cancer Res*  
1181 **2019**;79(2):311-9 doi 10.1158/0008-5472.CAN-18-1003.
- 1182 30. Chakraborty P, Grosse F. Human DHX9 helicase preferentially unwinds  
1183 RNA-containing displacement loops (R-loops) and G-quadruplexes. *DNA Repair*  
1184 (Amst) **2011**;10(6):654-65 doi 10.1016/j.dnarep.2011.04.013.
- 1185 31. Lee CG, Chang KA, Kuroda MI, Hurwitz J. The NTPase/helicase activities of

- 1186 *Drosophila* maleless, an essential factor in dosage compensation. *EMBO J*  
1187 **1997**;16(10):2671-81 doi 10.1093/emboj/16.10.2671.
- 1188 32. Lee T, Pelletier J. The biology of DHX9 and its potential as a therapeutic target.  
1189 *Oncotarget* **2016**;7(27):42716-39 doi 10.18632/oncotarget.8446.
- 1190 33. Choi H, Kwon J, Cho MS, Sun Y, Zheng X, Wang J, *et al.* Targeting DDX3X Triggers  
1191 Antitumor Immunity via a dsRNA-Mediated Tumor-Intrinsic Type I Interferon  
1192 Response. *Cancer Res* **2021**;81(13):3607-20 doi 10.1158/0008-5472.CAN-20-3790.
- 1193 34. Huang Y, Liu ZR. The ATPase, RNA unwinding, and RNA binding activities of  
1194 recombinant p68 RNA helicase. *J Biol Chem* **2002**;277(15):12810-5 doi  
1195 10.1074/jbc.M200182200.
- 1196 35. Bourgeois CF, Mortreux F, Auboeuf D. The multiple functions of RNA helicases as  
1197 drivers and regulators of gene expression. *Nat Rev Mol Cell Biol* **2016**;17(7):426-38  
1198 doi 10.1038/nrm.2016.50.
- 1199 36. Chellini L, Pieraccioli M, Sette C, Paronetto MP. The DNA/RNA helicase DHX9  
1200 contributes to the transcriptional program of the androgen receptor in prostate  
1201 cancer. *J Exp Clin Cancer Res* **2022**;41(1):178 doi 10.1186/s13046-022-02384-4.
- 1202 37. Shi F, Cao S, Zhu Y, Yu Q, Guo W, Zhang S. High expression of DHX9 promotes the  
1203 growth and metastasis of hepatocellular carcinoma. *J Clin Lab Anal*  
1204 **2021**;35(12):e24052 doi 10.1002/jcla.24052.
- 1205 38. Aktas T, Avsar Ilik I, Maticzka D, Bhardwaj V, Pessoa Rodrigues C, Mittler G, *et al.*  
1206 DHX9 suppresses RNA processing defects originating from the Alu invasion of the  
1207 human genome. *Nature* **2017**;544(7648):115-9 doi 10.1038/nature21715.
- 1208 39. Chen R, Ishak CA, De Carvalho DD. Endogenous Retroelements and the Viral  
1209 Mimicry Response in Cancer Therapy and Cellular Homeostasis. *Cancer Discov*  
1210 **2021**;11(11):2707-25 doi 10.1158/2159-8290.CD-21-0506.
- 1211 40. Sadeq S, Al-Hashimi S, Cusack CM, Werner A. Endogenous Double-Stranded RNA.  
1212 *Noncoding RNA* **2021**;7(1) doi 10.3390/ncrna7010015.
- 1213 41. Yu S, Jia M, Li Y, Sun PL, Gao H. Differential Expression of PD-L1 in Central and  
1214 Peripheral and TTF1-Positive and -Negative Small-Cell Lung Cancer. *Front Med*  
1215 (Lausanne) **2020**;7:621838 doi 10.3389/fmed.2020.621838.
- 1216 42. Patel PS, Abraham KJ, Guturi KKN, Halaby MJ, Khan Z, Palomero L, *et al.*  
1217 RNF168 regulates R-loop resolution and genomic stability in BRCA1/2-deficient  
1218 tumors. *J Clin Invest* **2021**;131(3) doi 10.1172/JCI140105.
- 1219 43. Cristini A, Groh M, Kristiansen MS, Gromak N. RNA/DNA Hybrid Interactome  
1220 Identifies DXH9 as a Molecular Player in Transcriptional Termination and  
1221 R-Loop-Associated DNA Damage. *Cell Rep* **2018**;23(6):1891-905 doi

- 1222 10.1016/j.celrep.2018.04.025.
- 1223 44. Crossley MP, Bocek M, Cimprich KA. R-Loops as Cellular Regulators and Genomic  
1224 Threats. *Mol Cell* **2019**;73(3):398-411 doi 10.1016/j.molcel.2019.01.024.
- 1225 45. Petermann E, Lan L, Zou L. Sources, resolution and physiological relevance of  
1226 R-loops and RNA-DNA hybrids. *Nat Rev Mol Cell Biol* **2022**;23(8):521-40 doi  
1227 10.1038/s41580-022-00474-x.
- 1228 46. Murayama T, Takeuchi Y, Yamawaki K, Natsume T, Li M, Marcela RN, *et al.*  
1229 MCM10 compensates for Myc-induced DNA replication stress in breast cancer  
1230 stem-like cells. *Cancer Sci* **2021**;112(3):1209-24 doi 10.1111/cas.14776.
- 1231 47. Collin G, Huna A, Warnier M, Flaman JM, Bernard D. Transcriptional repression of  
1232 DNA repair genes is a hallmark and a cause of cellular senescence. *Cell Death Dis*  
1233 **2018**;9(3):259 doi 10.1038/s41419-018-0300-z.
- 1234 48. Chen JH, Hales CN, Ozanne SE. DNA damage, cellular senescence and organismal  
1235 ageing: causal or correlative? *Nucleic Acids Res* **2007**;35(22):7417-28 doi  
1236 10.1093/nar/gkm681.
- 1237 49. Rudin CM, Durinck S, Stawiski EW, Poirier JT, Modrusan Z, Shames DS, *et al.*  
1238 Comprehensive genomic analysis identifies SOX2 as a frequently amplified gene in  
1239 small-cell lung cancer. *Nat Genet* **2012**;44(10):1111-6 doi 10.1038/ng.2405.
- 1240 50. Peifer M, Fernandez-Cuesta L, Sos ML, George J, Seidel D, Kasper LH, *et al.*  
1241 Integrative genome analyses identify key somatic driver mutations of small-cell lung  
1242 cancer. *Nat Genet* **2012**;44(10):1104-10 doi 10.1038/ng.2396.
- 1243 51. George J, Lim JS, Jang SJ, Cun Y, Ozretic L, Kong G, *et al.* Comprehensive genomic  
1244 profiles of small cell lung cancer. *Nature* **2015**;524(7563):47-53 doi  
1245 10.1038/nature14664.
- 1246 52. Doench JG, Fusi N, Sullender M, Hegde M, Vaimberg EW, Donovan KF, *et al.*  
1247 Optimized sgRNA design to maximize activity and minimize off-target effects of  
1248 CRISPR-Cas9. *Nat Biotechnol* **2016**;34(2):184-91 doi 10.1038/nbt.3437.
- 1249 53. Egloff S. CDK9 keeps RNA polymerase II on track. *Cell Mol Life Sci*  
1250 **2021**;78(14):5543-67 doi 10.1007/s00018-021-03878-8.
- 1251 54. Gorthi A, Romero JC, Loranc E, Cao L, Lawrence LA, Goodale E, *et al.* EWS-FLI1  
1252 increases transcription to cause R-loops and block BRCA1 repair in Ewing sarcoma.  
1253 *Nature* **2018**;555(7696):387-91 doi 10.1038/nature25748.
- 1254 55. Klusmann I, Wohlberedt K, Magerhans A, Teloni F, Korb J, Altmeyer M, *et al.*  
1255 Chromatin modifiers Mdm2 and RNF2 prevent RNA:DNA hybrids that impair DNA  
1256 replication. *Proc Natl Acad Sci U S A* **2018**;115(48):E11311-E20 doi  
1257 10.1073/pnas.1809592115.

- 1258 56. Yeo CQX, Alexander I, Lin Z, Lim S, Aning OA, Kumar R, *et al.* p53 Maintains  
1259 Genomic Stability by Preventing Interference between Transcription and  
1260 Replication. *Cell Rep* **2016**;15(1):132-46 doi 10.1016/j.celrep.2016.03.011.
- 1261 57. Lucking U, Scholz A, Lienau P, Siemeister G, Kosemund D, Bohlmann R, *et al.*  
1262 Identification of Atuveciclib (BAY 1143572), the First Highly Selective, Clinical  
1263 PTEFb/CDK9 Inhibitor for the Treatment of Cancer. *ChemMedChem*  
1264 **2017**;12(21):1776-93 doi 10.1002/cmde.201700447.
- 1265 58. Crossley MP, Bocek MJ, Hamperl S, Swigut T, Cimprich KA. qDRIP: a method to  
1266 quantitatively assess RNA-DNA hybrid formation genome-wide. *Nucleic Acids Res*  
1267 **2020**;48(14):e84 doi 10.1093/nar/gkaa500.
- 1268 59. Yuan W, Al-Hadid Q, Wang Z, Shen L, Cho H, Wu X, *et al.* TDRD3 promotes DHX9  
1269 chromatin recruitment and R-loop resolution. *Nucleic Acids Res* **2021**;49(15):8573-91  
1270 doi 10.1093/nar/gkab642.
- 1271 60. Oser MG, Sabet AH, Gao W, Chakraborty AA, Schinzel AC, Jennings RB, *et al.* The  
1272 KDM5A/RBP2 histone demethylase represses NOTCH signaling to sustain  
1273 neuroendocrine differentiation and promote small cell lung cancer tumorigenesis.  
1274 *Genes Dev* **2019**;33(23-24):1718-38 doi 10.1101/gad.328336.119.
- 1275 61. Paz-Ares L, Chen Y, Reinmuth N, Hotta K, Trukhin D, Statsenko G, *et al.*  
1276 Durvalumab, with or without tremelimumab, plus platinum-etoposide in first-line  
1277 treatment of extensive-stage small-cell lung cancer: 3-year overall survival update  
1278 from CASPIAN. *ESMO Open* **2022**;7(2):100408 doi 10.1016/j.esmoop.2022.100408.
- 1279 62. Owonikoko TK, Park K, Govindan R, Ready N, Reck M, Peters S, *et al.* Nivolumab  
1280 and Ipilimumab as Maintenance Therapy in Extensive-Disease Small-Cell Lung  
1281 Cancer: CheckMate 451. *Journal of clinical oncology : official journal of the*  
1282 *American Society of Clinical Oncology* **2021**;39(12):1349-59 doi  
1283 10.1200/JCO.20.02212.
- 1284 63. Ready NE, Ott PA, Hellmann MD, Zugazagoitia J, Hann CL, de Braud F, *et al.*  
1285 Nivolumab Monotherapy and Nivolumab Plus Ipilimumab in Recurrent Small Cell  
1286 Lung Cancer: Results From the CheckMate 032 Randomized Cohort. *J Thorac Oncol*  
1287 **2020**;15(3):426-35 doi 10.1016/j.jtho.2019.10.004.
- 1288 64. Park KS, Martelotto LG, Peifer M, Sos ML, Karnezis AN, Mahjoub MR, *et al.* A  
1289 crucial requirement for Hedgehog signaling in small cell lung cancer. *Nat Med*  
1290 **2011**;17(11):1504-8 doi 10.1038/nm.2473.
- 1291 65. Nishiga Y, Drinas AP, Baron M, Bhattacharya D, Barkal AA, Ahrari Y, *et al.*  
1292 Radiotherapy in combination with CD47 blockade elicits a macrophage-mediated  
1293 abscopal effect. *Nat Cancer* **2022**;3(11):1351-66 doi 10.1038/s43018-022-00456-0.



- 1294 66. Liu D, Schilling B, Liu D, Sucker A, Livingstone E, Jerby-Arnon L, *et al*. Integrative  
1295 molecular and clinical modeling of clinical outcomes to PD1 blockade in patients  
1296 with metastatic melanoma. *Nat Med* **2019**;25(12):1916-27 doi  
1297 10.1038/s41591-019-0654-5.
- 1298 67. Kim ST, Cristescu R, Bass AJ, Kim KM, Odegaard JI, Kim K, *et al*. Comprehensive  
1299 molecular characterization of clinical responses to PD-1 inhibition in metastatic  
1300 gastric cancer. *Nat Med* **2018**;24(9):1449-58 doi 10.1038/s41591-018-0101-z.
- 1301 68. Snyder A, Makarov V, Merghoub T, Yuan J, Zaretsky JM, Desrichard A, *et al*.  
1302 Genetic basis for clinical response to CTLA-4 blockade in melanoma. *N Engl J Med*  
1303 **2014**;371(23):2189-99 doi 10.1056/NEJMoa1406498.
- 1304 69. Lin YC, Yu YS, Lin HH, Hsiao KY. Oxaliplatin-Induced DHX9 Phosphorylation  
1305 Promotes Oncogenic Circular RNA CCDC66 Expression and Development of  
1306 Chemoresistance. *Cancers (Basel)* **2020**;12(3) doi 10.3390/cancers12030697.
- 1307 70. Chakraborty P, Huang JTJ, Hiom K. DHX9 helicase promotes R-loop formation in  
1308 cells with impaired RNA splicing. *Nat Commun* **2018**;9(1):4346 doi  
1309 10.1038/s41467-018-06677-1.
- 1310 71. Crossley MP, Song C, Bocek MJ, Choi JH, Kousorous J, Sathirachinda A, *et al*.  
1311 R-loop-derived cytoplasmic RNA-DNA hybrids activate an immune response. *Nature*  
1312 **2023**;613(7942):187-94 doi 10.1038/s41586-022-05545-9.
- 1313 72. Alexandrov LB, Nik-Zainal S, Wedge DC, Aparicio SA, Behjati S, Biankin AV, *et al*.  
1314 Signatures of mutational processes in human cancer. *Nature* **2013**;500(7463):415-21  
1315 doi 10.1038/nature12477.
- 1316 73. Iams WT, Porter J, Horn L. Immunotherapeutic approaches for small-cell lung  
1317 cancer. *Nat Rev Clin Oncol* **2020**;17(5):300-12 doi 10.1038/s41571-019-0316-z.
- 1318 74. Lee T, Paquet M, Larsson O, Pelletier J. Tumor cell survival dependence on the  
1319 DHX9 DExH-box helicase. *Oncogene* **2016**;35(39):5093-105 doi 10.1038/onc.2016.52.
- 1320 75. Jiao A, Sun C, Wang X, Lei L, Liu H, Li W, *et al*. DExD/H-box helicase 9 intrinsically  
1321 controls CD8(+) T cell-mediated antiviral response through noncanonical  
1322 mechanisms. *Sci Adv* **2022**;8(6):eabk2691 doi 10.1126/sciadv.abk2691.
- 1323 76. Wei X, Pacyna-Gengelbach M, Schluns K, An Q, Gao Y, Cheng S, *et al*. Analysis of  
1324 the RNA helicase A gene in human lung cancer. *Oncol Rep* **2004**;11(1):253-8 doi  
1325 10.3892/or.11.1.253.
- 1326 77. Sun Z, Wang L, Eckloff BW, Deng B, Wang Y, Wampfler JA, *et al*. Conserved  
1327 recurrent gene mutations correlate with pathway deregulation and clinical outcomes  
1328 of lung adenocarcinoma in never-smokers. *BMC Med Genomics* **2014**;7:32 doi  
1329 10.1186/1755-8794-7-32.

- 1330 78. Liu S, He L, Wu J, Wu X, Xie L, Dai W, *et al.* DHX9 contributes to the malignant  
1331 phenotypes of colorectal cancer via activating NF-kappaB signaling pathway. *Cell*  
1332 *Mol Life Sci* **2021**;78(24):8261-81 doi 10.1007/s00018-021-04013-3.
- 1333 79. Canadas I, Rojo F, Taus A, Arpi O, Arumi-Uria M, Pijuan L, *et al.* Targeting  
1334 epithelial-to-mesenchymal transition with Met inhibitors reverts chemoresistance in  
1335 small cell lung cancer. *Clin Cancer Res* **2014**;20(4):938-50 doi  
1336 10.1158/1078-0432.CCR-13-1330.
- 1337 80. Sanjana NE, Shalem O, Zhang F. Improved vectors and genome-wide libraries for  
1338 CRISPR screening. *Nat Methods* **2014**;11(8):783-4 doi 10.1038/nmeth.3047.
- 1339 81. Shalem O, Sanjana NE, Hartenian E, Shi X, Scott DA, Mikkelsen T, *et al.*  
1340 Genome-scale CRISPR-Cas9 knockout screening in human cells. *Science*  
1341 **2014**;343(6166):84-7 doi 10.1126/science.1247005.
- 1342 82. Bray NL, Pimentel H, Melsted P, Pachter L. Near-optimal probabilistic RNA-seq  
1343 quantification. *Nat Biotechnol* **2016**;34(5):525-7 doi 10.1038/nbt.3519.
- 1344 83. Langmead B, Salzberg SL. Fast gapped-read alignment with Bowtie 2. *Nat Methods*  
1345 **2012**;9(4):357-9 doi 10.1038/nmeth.1923.
- 1346 84. Criscione SW, Zhang Y, Thompson W, Sedivy JM, Neretti N. Transcriptional  
1347 landscape of repetitive elements in normal and cancer human cells. *BMC Genomics*  
1348 **2014**;15:583 doi 10.1186/1471-2164-15-583.
- 1349 85. Sanz LA, Chedin F. High-resolution, strand-specific R-loop mapping via S9.6-based  
1350 DNA-RNA immunoprecipitation and high-throughput sequencing. *Nat Protoc*  
1351 **2019**;14(6):1734-55 doi 10.1038/s41596-019-0159-1.
- 1352 86. Crossley MP, Cimprich KA. Quantitative DNA-RNA Immunoprecipitation  
1353 Sequencing with Spike-Ins. *Methods Mol Biol* **2022**;2528:381-410 doi  
1354 10.1007/978-1-0716-2477-7\_26.
- 1355 87. Sun Y, Sriramajayam K, Luo D, Liao DJ. A quick, cost-free method of purification of  
1356 DNA fragments from agarose gel. *J Cancer* **2012**;3:93-5 doi 10.7150/jca.4163.
- 1357 88. Li W, Xu H, Xiao T, Cong L, Love MI, Zhang F, *et al.* MAGeCK enables robust  
1358 identification of essential genes from genome-scale CRISPR/Cas9 knockout screens.  
1359 *Genome Biol* **2014**;15(12):554 doi 10.1186/s13059-014-0554-4.
- 1360 89. Hanzelmann S, Castelo R, Guinney J. GSEA: gene set variation analysis for  
1361 microarray and RNA-seq data. *BMC Bioinformatics* **2013**;14:7 doi  
1362 10.1186/1471-2105-14-7.
- 1363

1364 **Figure Legends**

1365 **Figure 1. DHX9 suppresses double-stranded RNA (dsRNA) accumulation in SCLCs**

1366 **A**, Schematic of the screen to identify critical regulators of dsRNA. Created with BioRender.com.

1367 **B**, Result of the dsRNA regulator screen. Relative mean fluorescence intensity (MFI) of dsRNA

1368 level in H446 cells depleted of RNA helicase genes was compared. **C**, DHX9 mRNA expression

1369 was profiled in 28 cancer types. The expression data of cancer cell lines (CCLE) were

1370 downloaded from cBioPortal and the cell lines were sub-grouped based on the information from

1371 Depmap database (sample\_info.csv, "Subtype"). In case "Subtype" information is not available,

1372 "primary\_disease", was used for sub-grouping. **D**, Analysis of DHX9 expression in indicated

1373 lung cancer (patient tumor) subtypes and normal lung. Data were downloaded from GEO

1374 database (GSE30219). Normal lung tissue (N = 14), LUAD (N = 85), LUSC (N = 61), LCNE (N

1375 = 56), SCLC (N = 20). Bars indicate the min and max values. **E**, Survival curve analysis of lung

1376 tumor patients. Data were downloaded from GEO database (GSE30219). **F**, Immunoblot (IB) of

1377 DHX9 protein in Scramble, sgDHX9 and sgDHX9 #2 H446 cells. **G**, Immunofluorescence

1378 images of dsRNA (red) staining of Scramble or sgDHX9 cells (treated w/wo RNase III). Nuclei

1379 were counterstained with DAPI. Scale bar = 10  $\mu$ m. **H**, Schematic (left) and result (right) of

1380 J2-RIP-seq analysis. Expression levels of specific retrotransposon classes (SINE, LINE, LTR) in

1381 Scramble or sgDHX9 cells are summarized (n = 3). CPM: Counts Per Million. **I**, Result of

1382 RIP-qRT-PCR analysis of the indicated retrotransposon elements (n = 3). 36B4 gene was used as

1383 a reference. **J**, RNA amounts which were pulled down with Flag antibody were compared among

1384 Flag-GFP-, Flag-MDA5-, and Flag-RIG-I-expressing cells. **K**, Schematic (left) and result (right)

1385 of sequencing analysis of RNA pulled down with Flag antibody. Expression levels of specific

1386 retrotransposon classes (SINE, LINE, LTR) are summarized (n = 3). CPM: Counts Per Million.

1387 **L**, Relative RNA amounts which were pulled down with Flag antibody were compared between

1388 3xFlag-DHX9-WT- and 3xFlag-DHX9-K417R-expressing cells. **M**, Sequencing analysis of

1389 RNA pulled down with Flag antibody. Expression levels of specific retrotransposon classes

1390 (SINE, LINE, LTR) are summarized (n = 3). CPM: Counts Per Million. **N**, Heatmap of

1391 Flag-RIP-seq results comparing DHX9, MDA5 and RIG-I bound RNA species (n = 3). rRNA:

1392 ribosomal RNA, srpRNA: signal recognition particle RNA, scRNA: small conditional RNA,

1393 snRNA: small nuclear RNA, tRNA: transfer RNA, RC: rolling circle, RNA: other RNA repeats,

1394 DNA: DNA repeat elements.

1395 Data represent mean  $\pm$  SEM. ns, not significant; \*p < 0.05, \*\*p < 0.01, \*\*\*p < 0.001, \*\*\*\*p <

1396 0.0001 by unpaired Student's t test (D, H, K and L), log-rank test (E), one-way ANOVA (J),

1397 two-way ANOVA followed by Tukey's multiple comparisons test (I).

1398

1399 **Figure 2. DHX9 depletion induces IFN response**

1400 **A**, Gene sets significantly upregulated and downregulated are shown, based on GSEA result.  
1401 Immune response related gene sets are in red, DNA damage related gene sets in pink and DNA  
1402 replication/cell cycle related gene sets in blue. **B**, GSEA analysis with C5 (ontology) gene sets,  
1403 based on RNA-seq results of sgDHX9 versus Scramble cells. **C**, qRT-PCR analysis of the  
1404 immune-related genes comparing Scramble and sgDHX9 H196 cells (n = 3). 36B4 gene was used  
1405 as a reference. **D**, Immunoblot (IB) of the indicated proteins in Scramble and sgDHX9 H196 cells.  
1406 **E**, ELISA of human IFN- $\beta$  protein in conditioned medium from Scramble and sgDHX9 H196  
1407 cells. **F**, Log2 fold change (FC) of cytokine/chemokine differences of sgDHX9 H196 compared  
1408 to Scramble. The cytokine/chemokine levels were quantified with Proteome Profiler Human  
1409 Cytokine Array Kit. **G and H**, Flow cytometry analysis of HLA-A.B.C (G) or PD-L1 (H)  
1410 expression on the cell surface of Scramble and sgDHX9 H196 cells. Data are representative of  
1411 three independent experiments (left). Mean fluorescence intensity (MFI) was quantified by  
1412 FlowJo (right) (n = 3). **I**, Schematic (top) and result (bottom) of qRT-PCR analysis of IFNB gene  
1413 in H196 cells treated with cytoplasmic dsRNA (n = 3). 36B4 gene was used as a reference.  
1414 Data represent mean  $\pm$  SEM. ns, not significant; \*p < 0.05, \*\*p < 0.01, \*\*\*p < 0.001, \*\*\*\*p <  
1415 0.0001 by unpaired Student's t test (C, E, G and H), one-way ANOVA (I).

1416

1417 **Figure 3. DHX9 depletion causes R-loop accumulation, DNA damage and cGAS-STING**  
1418 **pathway activation**

1419 **A**, GSEA analysis with C2 (curated) gene sets, based on RNA-seq results of sgDHX9 versus  
1420 Scramble cells. **B**, qRT-PCR analysis of the direct irradiation response and replication-related  
1421 genes comparing Scramble and sgDHX9 H196 cells (n = 3). 36B4 gene was used as a reference.  
1422 **C**, Immunofluorescence images of p-H2AX (red) staining of Scramble and sgDHX9 H196 cells.  
1423 Scale bar = 50  $\mu$ m. **D**, Flow cytometry analysis of intracellular p-H2AX levels in Scramble and  
1424 sgDHX9 H196 cells. Data are representative of three independent experiments (left). Mean  
1425 fluorescence intensity (MFI) was quantified by FlowJo (right) (n = 3). **E**, Immunofluorescence  
1426 images of DNA/RNA hybrid (red) staining of Scramble and sgDHX9 H196 cells (left) and  
1427 quantification of fluorescence intensity (right) (150 cells were counted per group, n = 3). Scale  
1428 bar = 50  $\mu$ m. **F**, Immunoblot (IB) of the indicated proteins in Scramble and sgDHX9 H196 cells.  
1429 **G**, DNA fiber assay of Scramble and sgDHX9 H196 cells. The percentage of stalled forks over  
1430 the total number of different replication structures was measured (>150 labeled forks were  
1431 counted per group, n = 3). **H**, Immunofluorescence images of dsDNA (green) and cGAS (red)  
1432 staining of Scramble and sgDHX9 H196 cells (left) and quantification of cells with  
1433 cGAS<sup>+</sup>-micronuclei (150 cells were counted per group, n = 3). Scale bar = 25  $\mu$ m. **I**, ELISA of  
1434 human cGAMP protein in Scramble and sgDHX9 H196 cells. **J**, Schematic (left) and result  
1435 (right) of qRT-PCR analysis of IFNB gene in H196 cells treated with cytoplasmic DNA (n = 3).  
1436 36B4 gene was used as a reference.  
1437 Data represent mean  $\pm$  SEM. ns, not significant; \*p < 0.05, \*\*p < 0.01, \*\*\*p < 0.001, \*\*\*\*p <  
1438 0.0001 by unpaired Student's t test (B, D, E, G, H and I), one-way ANOVA (J).

1439

1440 **Figure 4. DHX9 loss triggers dsRNA and dsDNA antiviral sensing pathways and IFN**  
1441 **signaling in SCLC cells**

1442 **A**, Growth curves of the indicated SCLC cell lines (n = 3). **B**, Flow cytometry analysis of  
1443 apoptotic (annexin V<sup>+</sup>) cells in Scramble and sgDHX9 H196 and H446 cells. Data are  
1444 representative of three independent experiments (left). Quantification of apoptotic cells is shown  
1445 (right) (n = 3). **C**, Growth curves of the indicated normal cell lines (n = 3). **D**, Flow cytometry  
1446 analysis of apoptotic (annexin V<sup>+</sup>) cells in Scramble and sgDHX9 FC1010 and RPE cells. Data  
1447 are representative of three independent experiments (left). Quantification of apoptotic cells is  
1448 shown (right) (n = 3). **E**, qRT-PCR analysis of the immune-related genes comparing Scramble  
1449 and sgSTING+sgMAVS H196 cells, transfected with siCtrl or siDHX9 (n = 3). 36B4 gene was  
1450 used as a reference. **F**, ELISA of human IFN- $\beta$  protein in conditioned medium from Scramble and  
1451 sgSTING+sgMAVS H196 cells, transfected with siCtrl or siDHX9 (n = 3). SM:  
1452 sgSTING+sgMAVS. **G**, Immunoblot (IB) of the indicated proteins in Scramble and  
1453 sgSTING+sgMAVS H196 cells, transfected with siCtrl or siDHX9. **H**, Growth curves of  
1454 Scramble and sgSTING+sgMAVS H196 cells, transfected with siCtrl or siDHX9 (n = 3).  
1455 Data represent mean  $\pm$  SEM. ns, not significant; \*p < 0.05, \*\*p < 0.01, \*\*\*p < 0.001, \*\*\*\*p <  
1456 0.0001 by unpaired Student's t test (A, B, C and D), two-way ANOVA followed by Tukey's  
1457 multiple comparisons test (E, F and H).

1458

1459 **Figure 5. CRISPR screen identifies modulators of sensitivity and resistance to DHX9 loss**  
1460 **A**, Schematic of the genome-wide CRISPR screening method to reveal regulators of DHX9  
1461 loss-related cell death. Created with BioRender.com. **B**, Top-rated enriched and depleted  
1462 sgRNAs from the genome-wide CRISPR screening are summarized. **C and D**, Gene ontology  
1463 analysis of sgRNA targeted genes of depleted (C) and enriched (D) in sgDHX9 population. **E**,  
1464 Relative cell number of Scramble and sgDHX9 H82 cells treated with DMSO or 0.5  $\mu$ M  
1465 BAY-1143572. Luminescence of CellTiter-Glo was detected on Day 5 after seeding (n = 3). **F**,  
1466 Immunoblot (IB) of the indicated proteins in Scramble and sgDHX9 H82 cells treated with  
1467 DMSO or 0.5  $\mu$ M BAY-1143572. **G**, DNA fiber assay of Scramble and sgDHX9 H82 cells  
1468 treated with DMSO or 0.5  $\mu$ M BAY-1143572. The percentage of stalled forks over the total  
1469 number of different replication structures was measured (>150 labeled forks were counted per  
1470 group, n = 3). **H**, Schematic model of growth rescue effect by CDK9 inhibition in DHX9 depleted  
1471 cells. Created with BioRender.com.  
1472 Data represent mean  $\pm$  SEM. ns, not significant; \*p < 0.05, \*\*p < 0.01, \*\*\*p < 0.001, \*\*\*\*p <  
1473 0.0001 by two-way ANOVA followed by Tukey's multiple comparisons test (E and G).  
1474

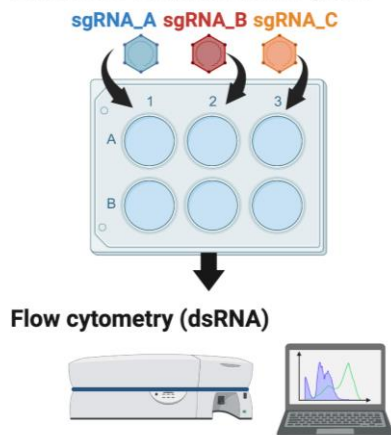
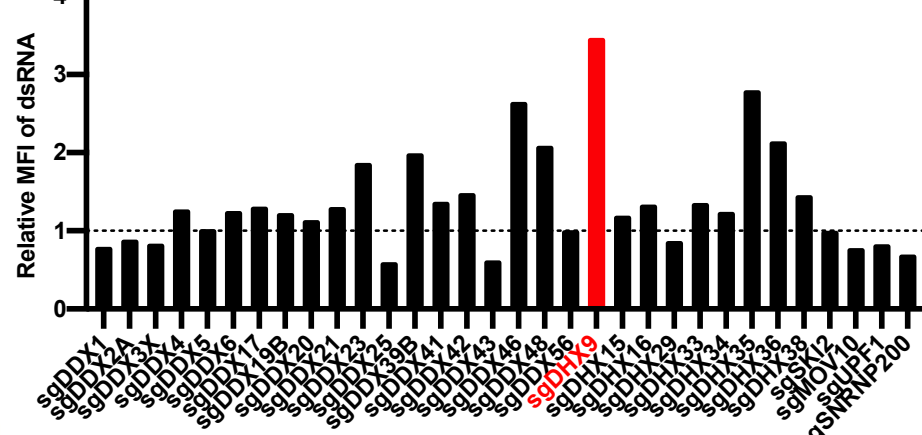
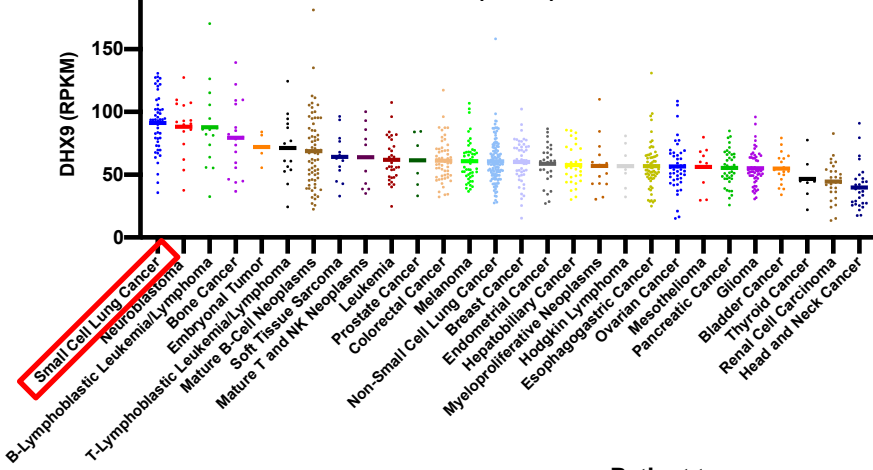
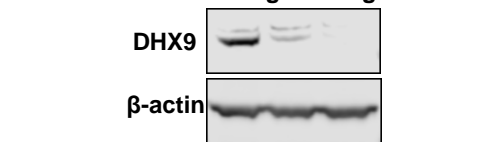
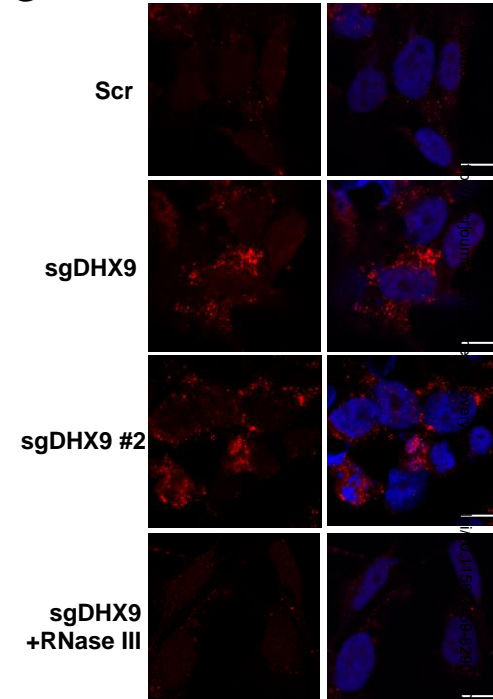
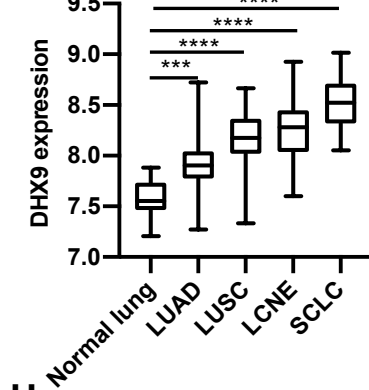
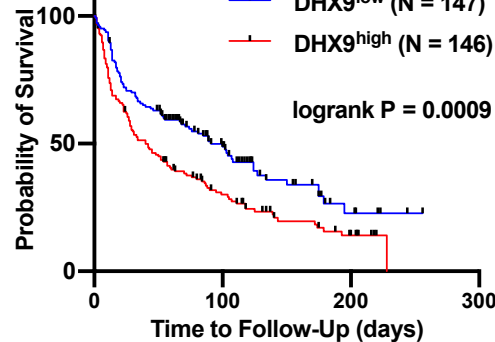
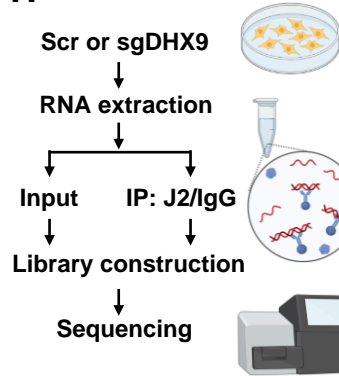
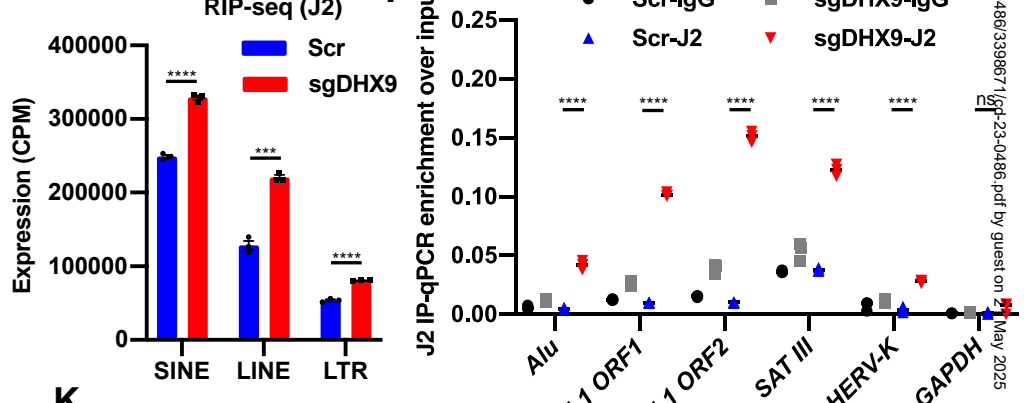
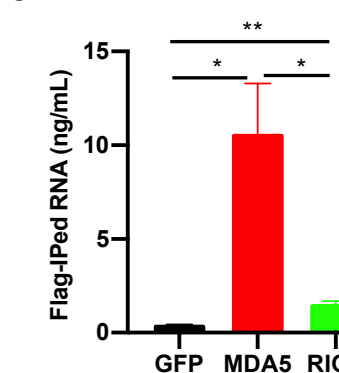
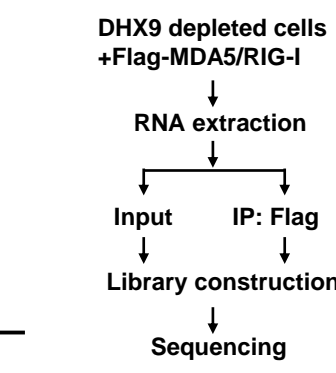
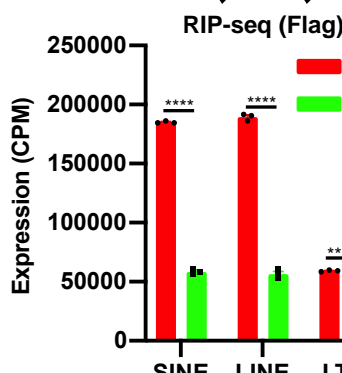
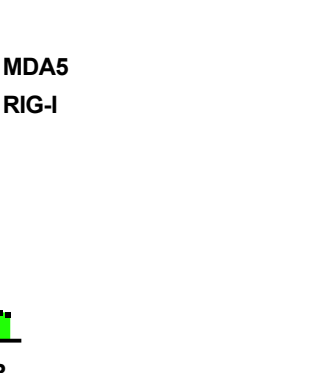
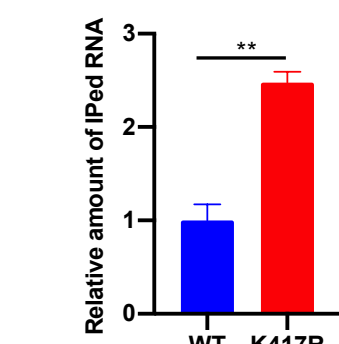
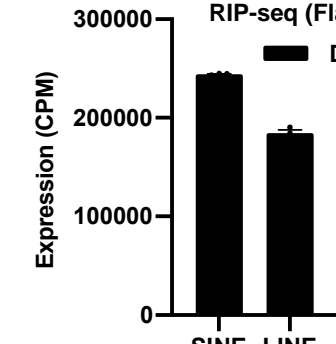
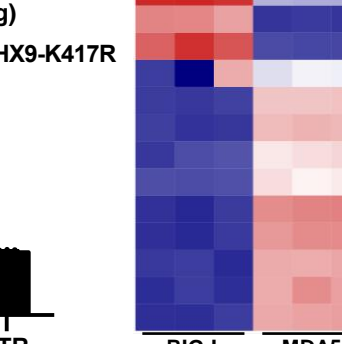
1475 **Figure 6. DHX9 depletion decreases tumor growth, induces immune cell infiltration and**  
1476 **enhances response to immune checkpoint blockade therapy**

1477 **A**, Schematic of *in vivo* tumor growth assay. RPP cells, which were transduced with  
1478 DOX-inducible shCtrl or shDhx9 vector, were transplanted into C57BL/6 mice. Created with  
1479 BioRender.com. **B and C**, Immunoblot (IB) (B) and qRT-PCR analysis (C) of DHX9 expression  
1480 in shCtrl and shDhx9 RPP cells treated w/wo DOX. **D**, Tumor growth curves of shCtrl and  
1481 shDhx9 RPP tumors (n = 6). **E**, Flow cytometry quantification of the indicated infiltrating  
1482 immune cells in shCtrl and shDhx9 RPP tumors. Each population was analyzed by FlowJo (n =  
1483 4). **F**, Flow cytometry quantification of infiltrating CD8<sup>+</sup> T cells and CD4<sup>+</sup> T cells of CD45<sup>+</sup>CD3<sup>+</sup>  
1484 cells in shCtrl and shDhx9 RPP tumors (n = 6). **G**, Representative IHC images of indicated  
1485 infiltrating immune cells in shCtrl and shDhx9 RPP tumors (left) and quantification (n = 6)  
1486 (right). Scale bar = 100  $\mu$ m. **H**, Tumor growth curves of shCtrl and shDhx9 RPP tumors treated  
1487 with isotype control or anti-PD-1 antibody (n = 9). **I**, Survival curves for mice in (H).  
1488 Data represent mean  $\pm$  SEM. ns, not significant; \*p < 0.05, \*\*p < 0.01, \*\*\*p < 0.001, \*\*\*\*p <  
1489 0.0001 by unpaired Student's t test (C, D, E, F and G), two-way ANOVA followed by Tukey's  
1490 multiple comparisons test (H) and log-rank test (I).

1491

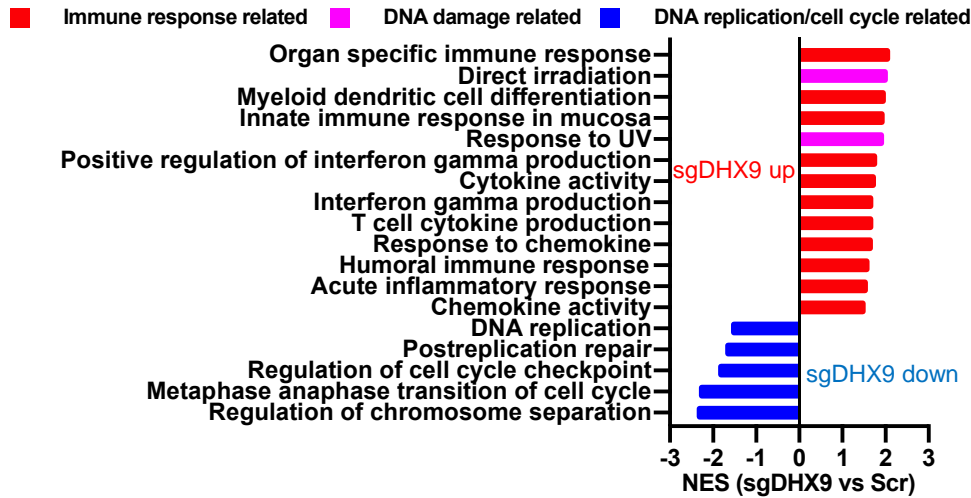


1492 **Figure 7. DHX9 is associated with poor clinical outcomes in cancer patient datasets**  
1493 **A**, Representative IHC images of DHX9 expression in SCLC tumors and normal lung tissue. **B**,  
1494 Quantification of IHC images of DHX9 in (A). Normal lung tissue (N = 10), Stage I (N = 9),  
1495 Stage II (N = 23), Stage III (N = 8). **C**, GSEA analysis with H (hallmark) gene sets, based on  
1496 RNA-seq results of 81 SCLC patient tumors (N = 40 DHX9<sup>low</sup> versus N = 41 DHX9<sup>high</sup>). Data  
1497 were downloaded from cBioPortal (U Cologne, Nature 2015 (51)). **D**, Gene ontology analysis of  
1498 genes upregulated in DHX9<sup>low</sup> lung patient tumors. Data were downloaded from TCGA. **E**,  
1499 Correlation analysis between DHX9 expression level and z-scores of the indicated gene sets in  
1500 different tumor types of TCGA (patient tumors). **F**, Boxplots of DHX9-depleted signature  
1501 z-scores in non-responder and responder of patients treated with immune checkpoint blockade  
1502 therapy, to anticipate the potential clinical relevance of targeting DHX9 in immunotherapy  
1503 settings. The DHX9-depleted gene signature was prepared based on genes upregulated in  
1504 sgDHX9 SCLC cells when compared to scramble and includes the two most prominent features  
1505 of DHX9 depleted cells: DNA damage response and immune response. **G**, Schematic model of  
1506 antitumor effects caused by DHX9 inhibition. Created with BioRender.com.  
1507 Data represent mean ± SEM. ns, not significant; \*p < 0.05, \*\*p < 0.01, \*\*\*p < 0.001, \*\*\*\*p <  
1508 0.0001 by one-way ANOVA (B) and unpaired Student's t test (F).  
1509

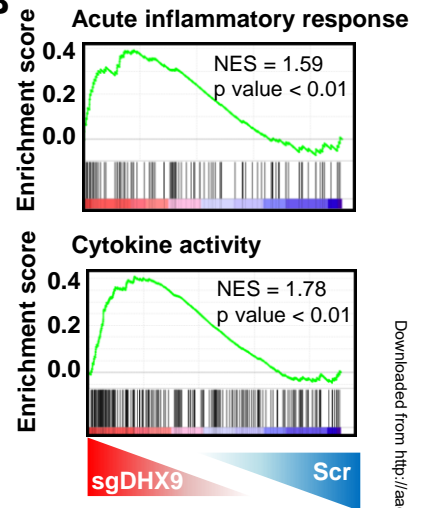
**Figure 1****A CRISPR KO of RNA helicase genes****B****C Pan-cancer (CCLE); Cell lines****F****G****D GSE30219; Patient tumors****E Patient tumors****H****I****J****K****L****M****N****O****P**

# Figure 2

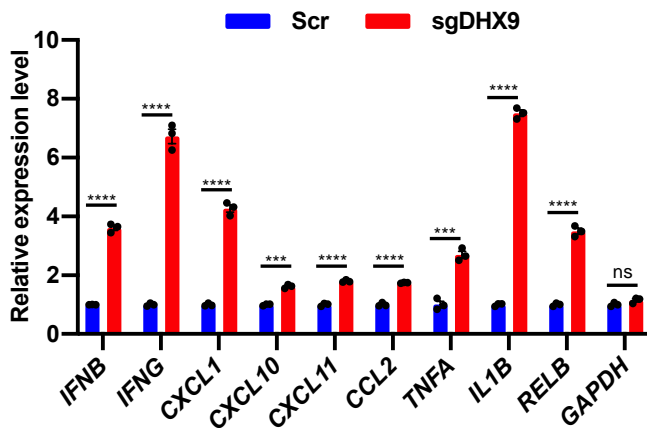
**A**



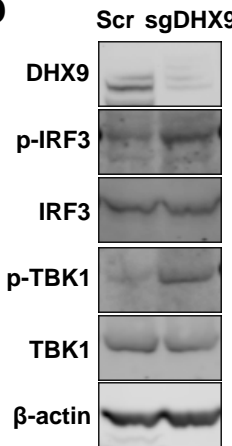
**B**



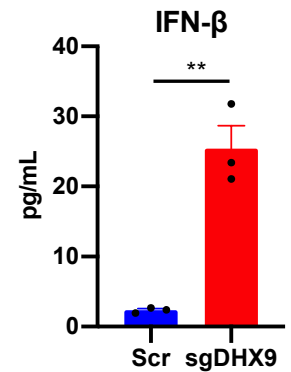
**C**



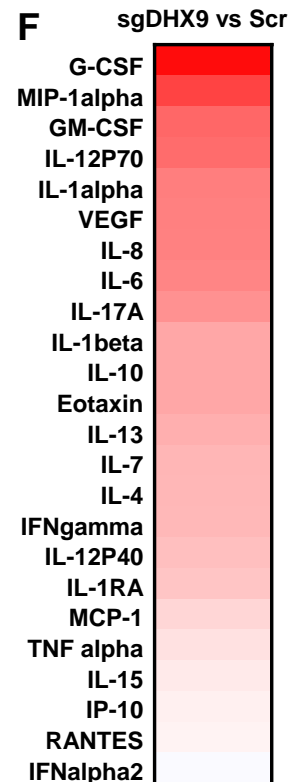
**D**



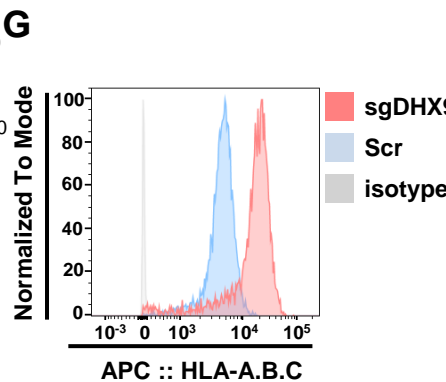
**E**



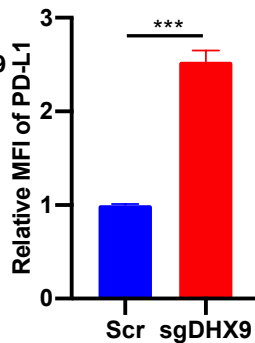
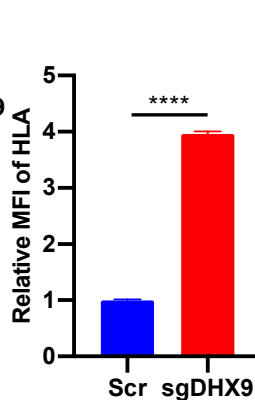
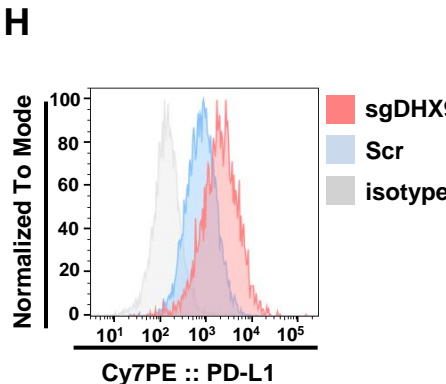
**F**



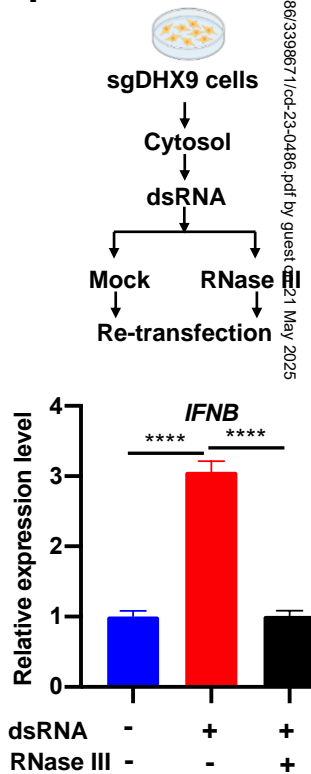
**G**



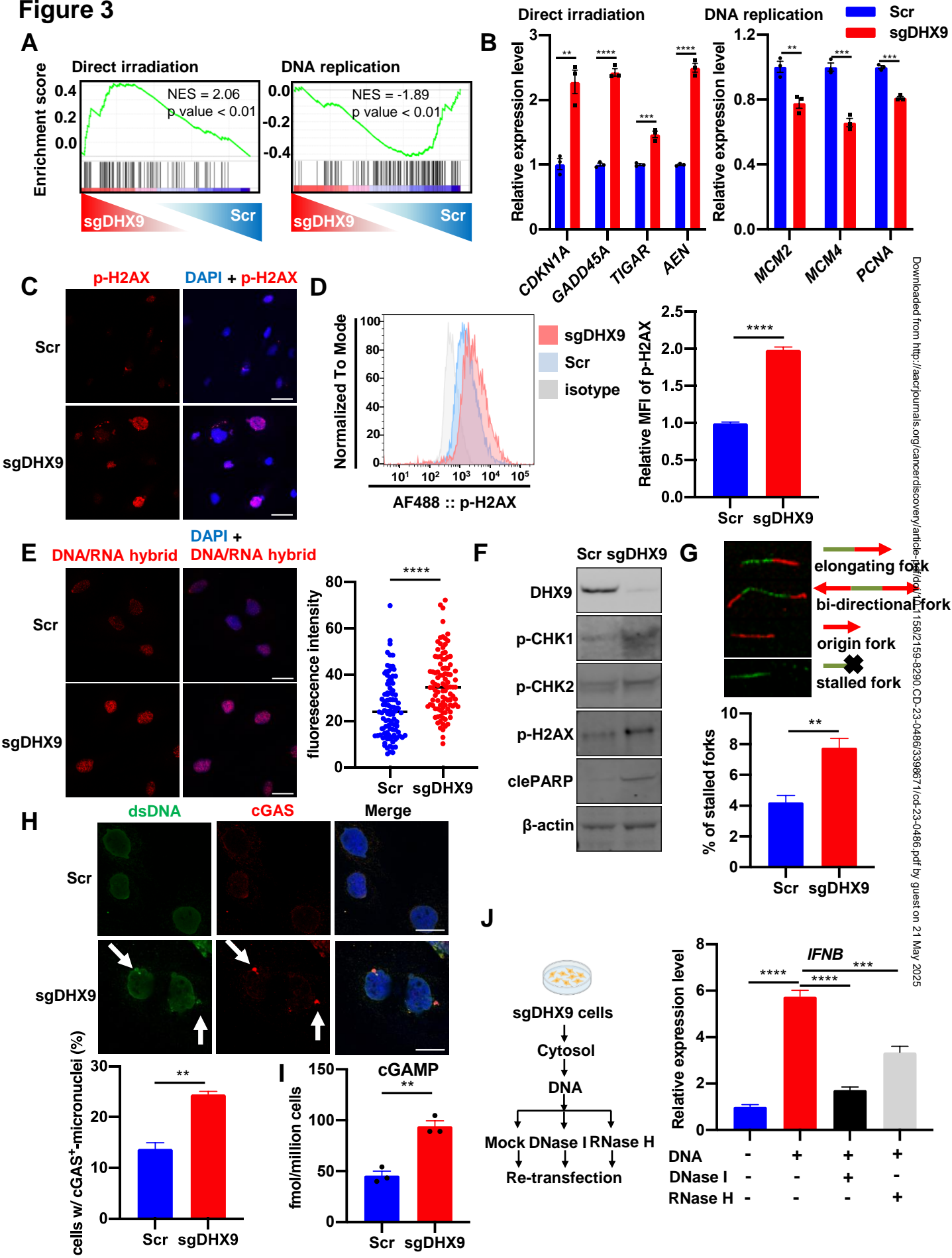
**H**



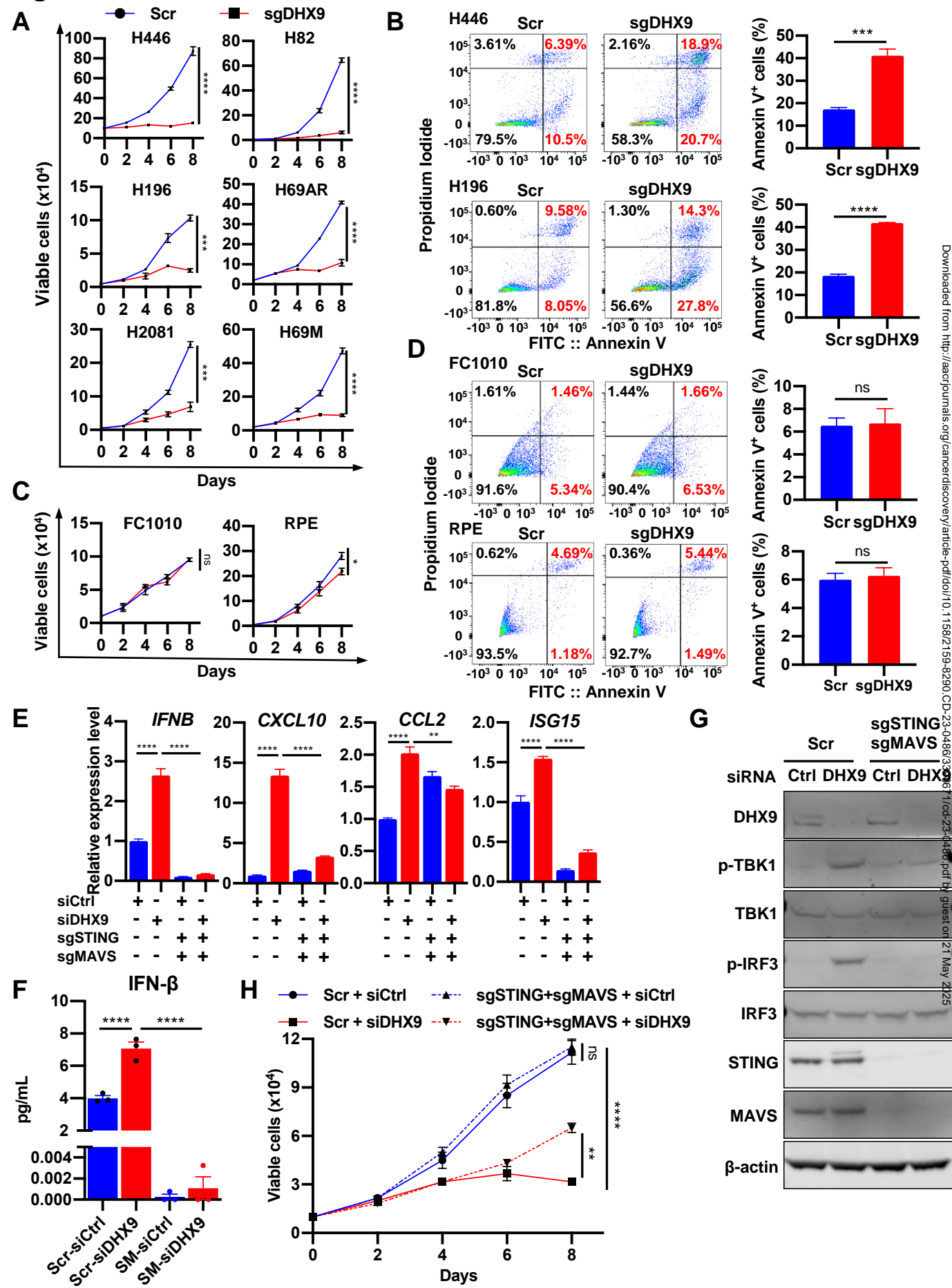
**I**



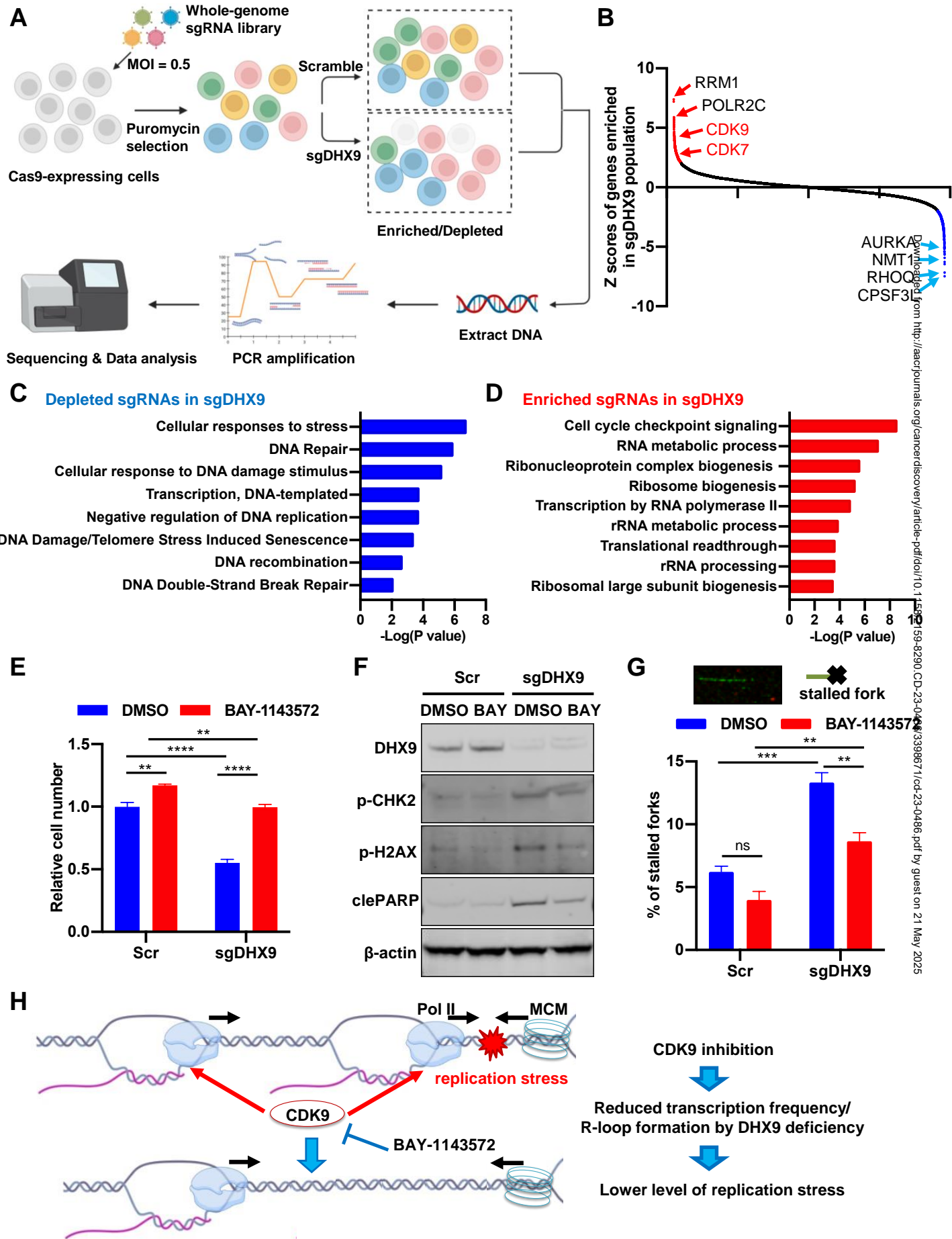
**Figure 3**



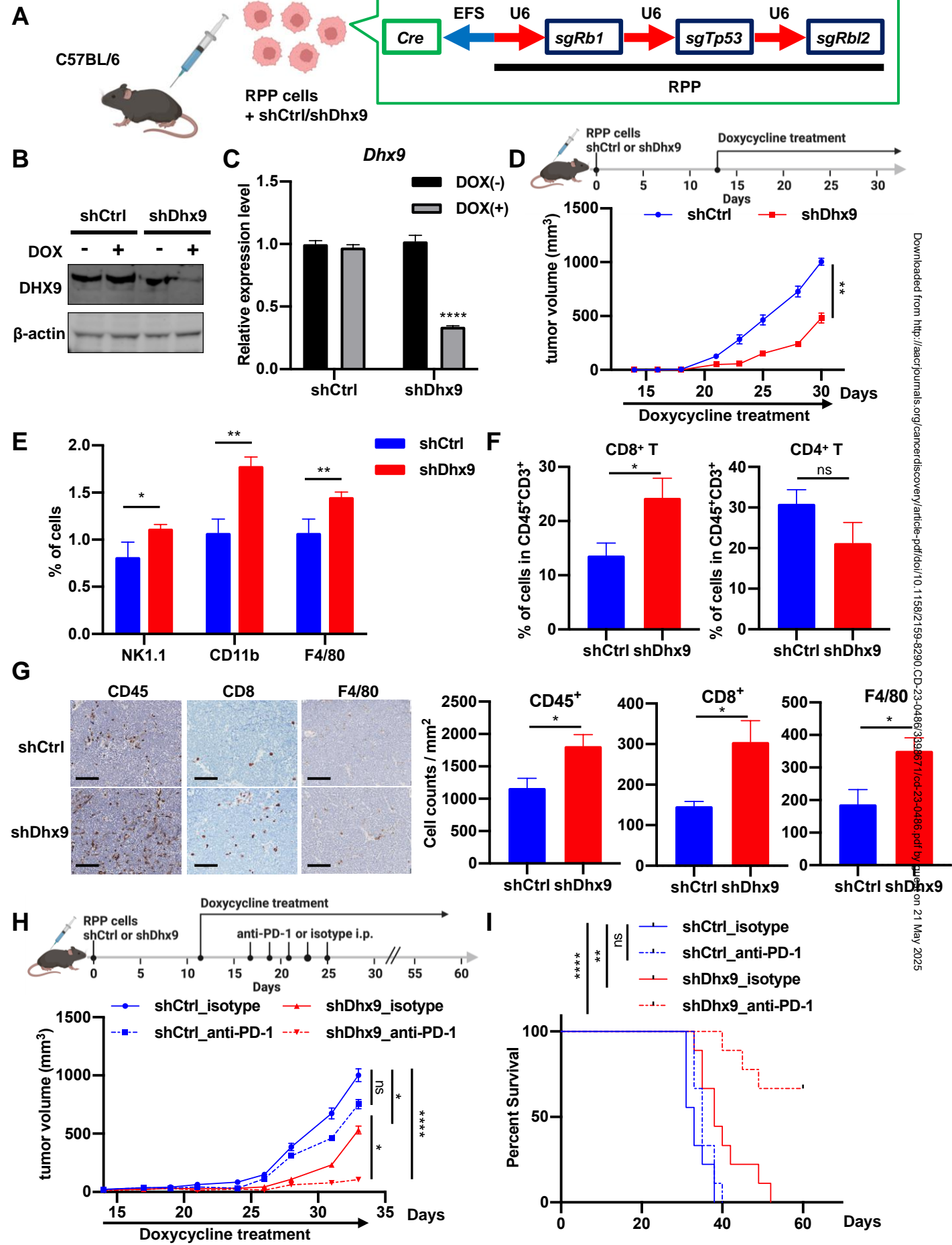
**Figure 4**

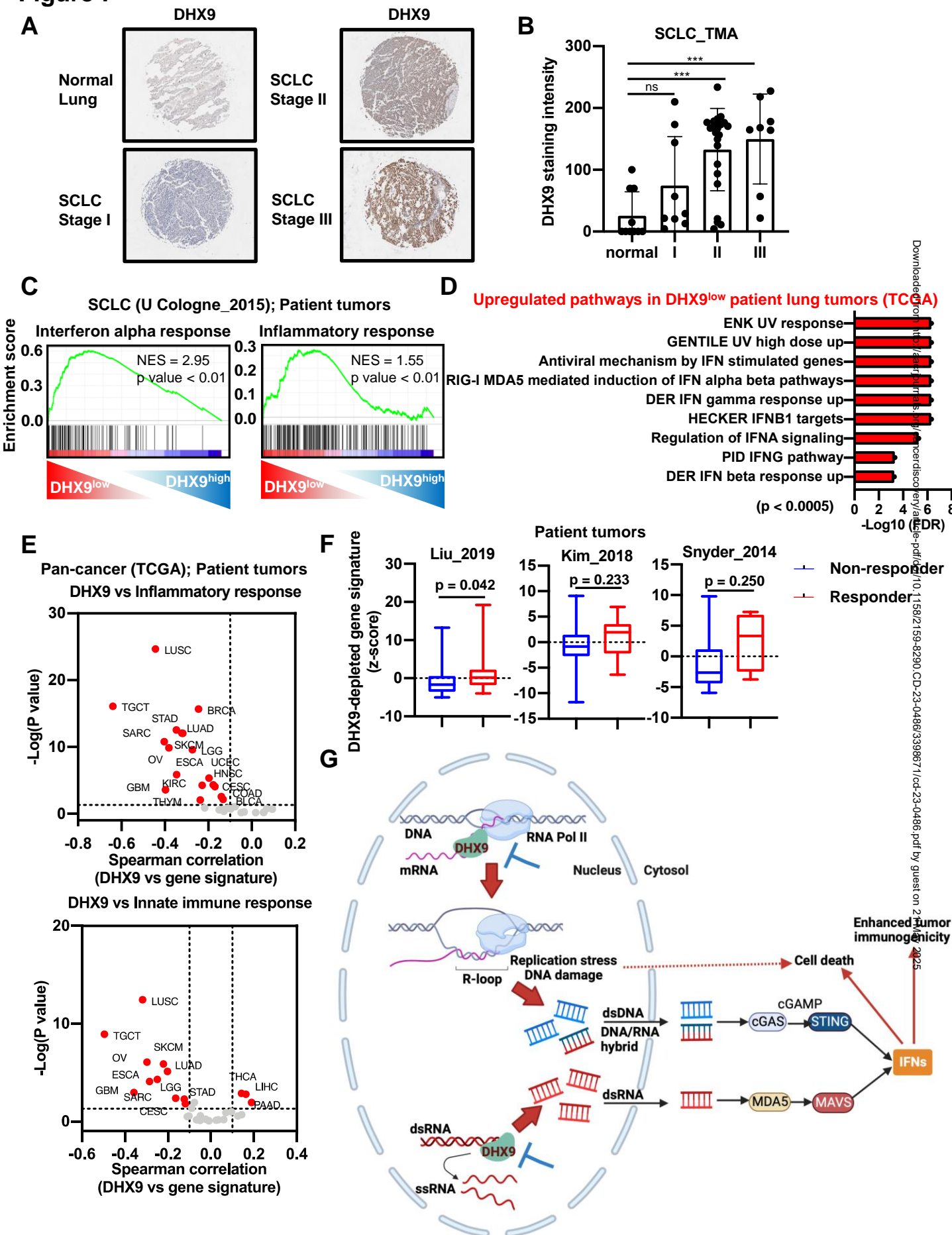


# Figure 5



# Figure 6



**Figure 7**

Downloaded from <http://eic.oxfordjournals.org/> by guest on 21 March 2025